

QUASI-PERIODIC INWARD SHOCK FORMATIONS IN THE SYSTEM OF A BLACK HOLE AND AN ACCRETION DISK AND APPLICATION TO QUASI-PERIODIC OSCILLATIONS IN GALACTIC BLACK HOLE CANDIDATES

SEIICHIRO I. AOKI

Kwasan and Hida Observatories, Kyoto University, Yamashina, Kyoto 607-8471, Japan; Department of Astronomy, Faculty of Science,
University of Tokyo, 7-3-1 Hongo, Bunkyo-ku, Tokyo 113-0033, Japan; and Solar Division, National Astronomical Observatory,
2-21-1 Osawa, Mitaka, Tokyo 181-8588, Japan; aoki@kwasan.kyoto-u.ac.jp

SHINJI KOIDE

Department of Engineering, Toyama University, 3190 Gofuku, Toyama 930-8555, Japan; koidesin@eng.toyama-u.ac.jp

TAKAHIRO KUDOH

Department of Physics and Astronomy, University of Western Ontario, London, ON N6A 3K7, Canada; kudoh@astro.uwo.ca

KUNJI NAKAYAMA

Faculty of Law, Ryukoku University, Fushimi-ku, Kyoto 612-8577, Japan; nakayama@law.ryukoku.ac.jp

AND

KAZUNARI SHIBATA

Kwasan and Hida Observatories, Kyoto University, Yamashina, Kyoto 607-8471, Japan; shibata@kwasan.kyoto-u.ac.jp

Received 2003 October 10; accepted 2004 April 5

ABSTRACT

We performed 1.5-dimensional general relativistic hydrodynamic simulations with a Kerr metric to construct a model for high-frequency quasi-periodic oscillations (QPOs) in microquasars. The simulations were performed assuming an initial accretion disk without viscosity rotating around a Kerr black hole at sub-Keplerian velocity (sub-Keplerian case), which induces various wave modes everywhere in the disk. We found that quasi-periodic inward shock waves propagate from the accretion disk toward the black hole. The frequency of the shock formation is about the maximum epicyclic frequency in the disk (κ_{\max}), which depends on the rotation of the black hole. In order to understand the mechanism of the shock formation, we also performed a simulation assuming an initial linear perturbation injected at one point in the Keplerian disk (linear perturbation case) and found an oscillation with frequency $\sim\kappa$ at the point where the perturbation injection occurred. To explain the simulation result, we derived an analytic solution for the time evolution of the linear perturbation of physical variables near the point of the perturbation injection and found that the time evolution of the oscillation can be described well. From comparison of the result in the sub-Keplerian case with that of the linear perturbation case, we found that the periodicity of the quasi-periodic shock formation in the sub-Keplerian case is due to a filtering effect by the epicyclic frequency distribution in the disk, which acts on the wave propagation toward the black hole. The only necessary condition for quasi-periodic shock formation is having a nonsteady character for the disks, which can be a source of acoustic waves. The frequency of the shock formation ($\sim\kappa_{\max}$) is on the order of the frequency of the high-frequency QPOs in microquasars and depends on the rotation of the black hole. Hence, we can estimate the spin parameter (a) of a black hole candidate (BHC) in a microquasar by comparing the frequency of the high-frequency QPO with κ_{\max} . The spin parameters of the BHCs in microquasars are roughly estimated to be $a = 0.345 \pm 0.345$ for GRS 1915+105 and $a = 0.895 \pm 0.105$ for GRO J1655–40.

Subject headings: accretion, accretion disks — black hole physics — hydrodynamics — methods: numerical — relativity

1. INTRODUCTION

The time variations of the various physical quantities of astrophysical objects reveal much about the nature of those objects. The time variation of intensity is one of them. Quasi-periodic oscillations (QPOs) are found from the analysis of power spectra of the intensity variations. Since their discovery, QPOs have been found in various astrophysical classes, such as Galactic X-ray binaries (see van der Klis 2000 for a recent review), X-ray novae (Rosen et al. 1995; Beardmore & Osborne 1997; Morales-Rueda et al. 1999), X-ray pulsars (see Takeshima et al. 1994 and references therein), microquasars (Morgan et al. 1997; Cui et al. 1999; Markwardt et al. 1999; Remillard et al. 1999a, 1999b; Sobczak et al. 1999), active

galactic nuclei (Fiore et al. 1989; Mittaz & Branduardi-Raymont 1989), and cataclysmic variables (Patterson et al. 1977; Middleditch 1982). Moreover, the QPOs associated with black hole candidates (BHCs) show high-frequency components on the order of 100 Hz (Morgan et al. 1997; Homan et al. 1999, 2001; Remillard et al. 1999a, 1999b) and low-frequency components on the order of 1 Hz (Morgan et al. 1997; Cui et al. 1999; Sobczak et al. 2000).

We can divide QPOs into two classes depending on whether or not the central objects are BHCs. A black hole does not have a solid surface, so the accretion disk around a black hole is possibly crucial for the origin of QPOs. There are two models of QPOs associated with BHCs, the Lense-Thirring (Lense & Thirring 1918) model (Cui et al. 1998; Stella &

Vietri 1998; Merloni et al. 1999; Stella et al. 1999) and the disk-oscillation model (Kato & Fukue 1980; Kato 1989, 1990, 2001; Nowak et al. 1997; Nowak & Wagoner 1991, 1992; Perez et al. 1997; Kato et al. 1998; Nowak & Lehr 1998; Wagoner 1999). The Lense-Thirring model explains QPOs by arguing that they are due to the precession of the disk in the ergosphere around a Kerr black hole, which occurs when the rotation axis of the disk is not parallel to that of the black hole. On the other hand, in the disk-oscillation model, QPOs have been explained by oscillations in the disk due to coherent waves. In this model, acoustic waves are produced by the viscosity of the disk, and they are trapped and amplified near the inner edge. Then, a coherent wave is produced. The frequency of the coherent wave becomes about the maximum epicyclic frequency (κ_{\max}) in the disk. Here we note that QPOs in the objects associated with BHCs cannot be explained by a beat-frequency-modulated accretion model (Alpar & Shaham 1985; Lamb et al. 1985), which has been proposed for QPOs associated with neutron stars. This is because there is no solid surface for a black hole, and a magnetic field line cannot be stably anchored.

Numerical studies of QPOs based on the disk-oscillation model have been performed by Matsumoto et al. (1988, 1989), Honma et al. (1992), and Chen & Taam (1995) using 1.5-dimensional hydrodynamic simulations including disk viscosity. They infer from their results that acoustic waves are trapped and amplified near the inner edge of the disk as a result of disk viscosity. In their simulations, coherent inward and outward (shock) waves are produced. The frequencies of the waves are $\sim \kappa_{\max}$, as predicted by the disk-oscillation model. Moreover, 2.5-dimensional hydrodynamic simulations have been performed by Milsom & Taam (1997), and oscillations with frequency $\sim \kappa_{\max}$ have been observed. In all their simulations, disk viscosity is necessary for amplifying waves and producing coherent inward and outward (shock) waves with frequency $\sim \kappa_{\max}$, where κ_{\max} is on the order of the frequencies in high-frequency QPOs in microquasars (~ 100 Hz).

The above simulations were performed including the α -viscosity of the disk assumed in the standard disk model (Shakura & Sunyaev 1973). The α -viscosity is necessary for the amplification of acoustic waves and oscillation with frequency $\sim \kappa_{\max}$ in their simulation. Although it has been supposed that the origin of α -viscosity is magnetic viscosity in the disk (Balbus & Hawley 1991; Brandenburg et al. 1995; Hawley et al. 1995; Matsumoto & Tajima 1995; Machida et al. 2000), it has not been resolved whether or not acoustic waves are amplified by magnetic viscosity. We think the disk viscosity is not crucial to producing oscillations in an accretion disk, so we exclude the viscosity of the disk in our simulations. In addition, the previous simulations were performed with a pseudo-Newtonian potential (Paczynsky & Wiita 1980). The epicyclic frequency (κ) distribution near the black hole with a pseudo-Newtonian potential is quite different from that with a fully general relativistic treatment (Fig. 1). Moreover, κ_{\max} largely depends on the spin parameter of the black hole, which directly relates to the rotation of the black hole. Hence, if we want to investigate the mechanism of high-frequency QPOs in detail, studying the oscillations in the disk, a fully general relativistic treatment is necessary. Thus, to explain the mechanism of high-frequency QPOs, we performed general relativistic hydrodynamic (GRHD) simulations under a Kerr metric without disk viscosity.

In § 2 we show the models, basic equations, numerical method, parameters, and initial and boundary conditions in our

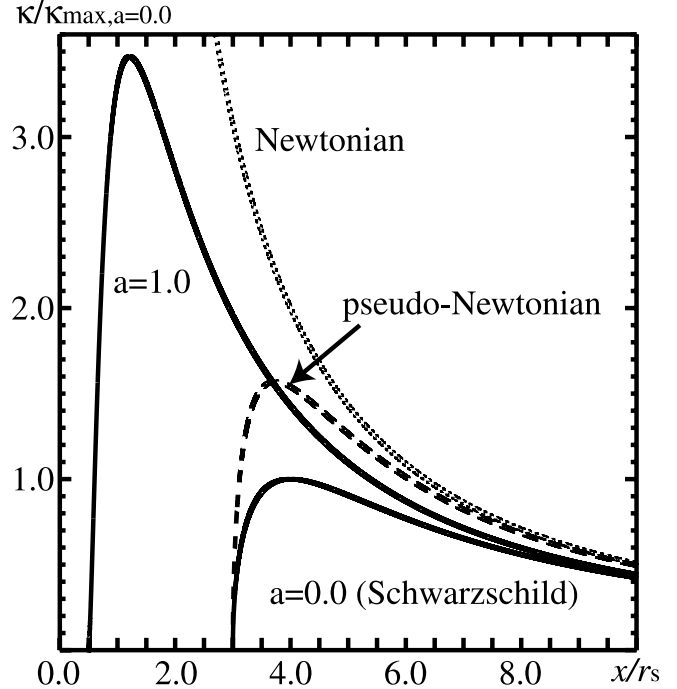


FIG. 1.—Distributions of the epicyclic frequency in an accretion disk around a black hole. The horizontal axis shows the distance from the central black hole in units of the Schwarzschild radius (r_s), whereas the vertical axis shows the frequency in units of the maximum epicyclic frequency in the disk around a Schwarzschild black hole ($\kappa_{\max, a=0.0}$). The distributions of the epicyclic frequencies in the disk in the general relativistic treatment (κ) are shown by solid curves ($a = 0.0, 1.0$, where a is the spin parameter of the black hole). It can be seen that the distribution and the maximum value of κ largely depend on the spin parameter of the black hole. In the nonrelativistic limit, there is no finite maximum value, as shown by the dotted curve. The dashed curve shows the case of a pseudo-Newtonian potential. There is also a maximum value for the distribution of κ in the pseudo-Newtonian case, which is ~ 1.6 times $\kappa_{\max, a=0.0}$. However, the distribution of κ near the black hole is quite different from that in the general relativistic treatment.

simulations. The results of the simulations are shown in § 3. Then we discuss the mechanism of the production of the quasi-periodic inward shock waves and compare our result with the high-frequency QPOs in microquasars in § 4.

2. METHOD

2.1. Model

We modeled a black hole and an accretion disk in order to apply the oscillations in the disk to high-frequency QPOs in microquasars, and performed 1.5-dimensional axially symmetric GRHD simulations in the equatorial plane of the disk (Fig. 2). The 1.5 dimensions mean that the spatial coordinate is in one dimension (radial direction), whereas the velocity has two (radial and azimuthal) components. The metric is static, determined only by the black hole (self-gravity of the disk is neglected). We assume that the plasma is an adiabatic non-viscous gas (the specific heat ratio is taken as $\Gamma = 5/3$). We examined four cases for the spin parameter of the black hole ($a \equiv J/J_{\max} = J/Mr_g c = cJ/GM^2$, where J is the angular momentum of the black hole and $r_g = GM/c^2$): (1) a non-rotating black hole ($a = 0.0$) and black holes rotating at (2) 90%, (3) 95%, and (4) 99% of the maximum rotation ($a = 0.90, a = 0.95, a = 0.99$). In this paper we show the results of the simulations for the cases of $a = 0.0$ and $a = 0.99$ in detail. Here we define x as the radius from a black

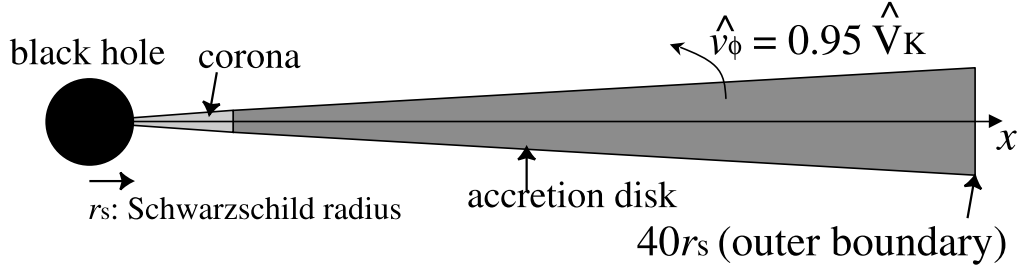


FIG. 2.—Schematic view of our model. The filled circle at the left indicates the black hole, whereas the dark-gray area at the right indicates the accretion disk in the region $3.0 \leq x/r_S \leq 40.0$ (nonrotating black hole case: $a = 0.0$) or $0.73 \leq x/r_S \leq 40.0$ (rapidly rotating black hole case: $a = 0.99$). The region between the black hole and the disk is filled with the disk corona, indicated by the light-gray area. There are 1500 mesh points in the simulation area of $1.2 \leq x/r_S \leq 40.0$ in the $a = 0.0$ case, whereas 2500 mesh points are included in the simulation area of $0.59 \leq x/r_S \leq 40.0$ in the $a = 0.99$ case. The initial rotation of the disk is taken as sub-Keplerian: $\hat{v}_\phi/\hat{V}_K = 0.95$. The inner and outer boundaries are assumed to be free boundaries.

hole in units of the Schwarzschild radius. In the $a = 0.0$ case, we performed the simulation in the region $1.2r_S \leq x \leq 40.0r_S$ with 1500 mesh points (with the horizon of the black hole at $x = 1.0r_S$). On the other hand, in the $a = 0.99$ case, the simulation was performed in the region $0.59r_S \leq x \leq 40.0r_S$ with 2500 mesh points (with the horizon of the black hole at $x \simeq 0.57r_S$). Mesh sizes increase exponentially with the distance from the black hole (tortoise coordinates).

2.2. Basic Equations

Our GRHD simulations were performed using basic equations in conservative form written in the 3+1 formalism (Thorne et al. 1986). The code used in our simulation was developed by Koide et al. (1998, 2000). The details of the basic equations and numerical method in our simulations have been described by Koide (2003).

The basic equations such as mass and energy-momentum conservation laws written in covariant form are

$$\nabla_\nu(\rho U^\nu) = 0, \quad (1)$$

$$\nabla_\nu T^{\mu\nu} = 0, \quad (2)$$

respectively, where ∇_ν is the covariant derivative, U^ν is the four-velocity, and $T^{\mu\nu}$ is the general relativistic energy-momentum tensor, given by

$$T^{\mu\nu} = pg^{\mu\nu} + (e_{\text{int}} + p)U^\mu U^\nu, \quad (3)$$

where ρ , p , and e_{int} are the proper mass density, proper pressure, and proper internal energy density [$e_{\text{int}} = \rho c^2 + p/(\Gamma - 1)$]. We use subscripts or superscripts of Greek letters to represent four-dimensional spacetime ($\mu, \nu = 0, 1, 2, 3$) and of Latin letters to represent three-dimensional space ($i, j = 1, 2, 3$).

The line element in Boyer-Lindquist (Boyer & Lindquist 1967) coordinates is written as

$$\begin{aligned} (ds)^2 &= g_{\mu\nu} dx^\mu dx^\nu \\ &= g_{00}(c dt)^2 + g_{03} c dt d\phi \\ &\quad + g_{11} dr^2 + g_{22} d\theta^2 + g_{33} d\phi^2, \end{aligned} \quad (4)$$

where the elements of the metric $g_{\mu\nu}$ are given by

$$\begin{aligned} g_{00} &\equiv -h_0^2, & g_{ii} &\equiv h_i^2, \\ g_{i0} &= g_{0i} \equiv -h_i^2 \omega_i / c, \end{aligned} \quad (5)$$

and the other elements vanish. Here $h_0 = (1 - 2r_g r / \Sigma)^{1/2}$, $h_1 = (\Sigma / \Delta)^{1/2}$, $h_2 = \Sigma^{1/2}$, $h_3 = (A / \Sigma)^{1/2} \sin \theta$, $\omega_1 = \omega_2 = 0$, $\omega_3 = 2cr_g^2 ar / A$ [$r_g = (1/2)r_S = GM/c^2$, where r_S is the Schwarzschild radius], $\Delta = r^2 - 2r_g r + (ar_g)^2$, $\Sigma = r^2 + (ar_g)^2 \cos^2 \theta$, and $A = [r^2 + (ar_g)^2]^2 - \Delta (ar_g)^2 \sin^2 \theta$. In this metric, the lapse function is represented by

$$\alpha = \sqrt{\frac{\Delta \Sigma}{A}} = \sqrt{h_0^2 + \sum_{i=1}^3 \left(\frac{h_i \omega_i}{c} \right)^2}. \quad (6)$$

The radial position of the event horizon and the surface of the ergosphere are given by $r_H = r_g [1 + (1 - a^2)^{1/2}]$ and $r_{\text{ergo}} = r_g [1 + (1 - a^2 \cos^2 \theta)^{1/2}]$, respectively.

Using h_μ and ω_i , the line element (ds) can be rewritten as

$$(ds)^2 = g_{\mu\nu} dx^\mu dx^\nu \quad (7)$$

$$= -h_0^2 (c dt)^2 + \sum_{i=1}^3 \left[h_i^2 (dx^i)^2 - 2h_i^2 \omega_i dt dx^i \right] \quad (8)$$

$$= -\alpha^2 (c dt)^2 + \sum_{i=1}^3 (h_i dx^i - c\beta^i \alpha dt)^2, \quad (9)$$

where the shift vector β^i is defined by

$$\beta^i = \frac{h_i \omega_i}{c\alpha}. \quad (10)$$

From the basic equations written in covariant form, we now rewrite the basic equations in the 3+1 formalism. In this formalism, we define the scalars in a comoving frame. The vectors are defined with respect to a fiducial observer (FIDO), who is at rest relative to the black hole. We assume that the coordinates in the FIDO frame are given by $(\hat{c}\hat{t}, \hat{x}^1, \hat{x}^2, \hat{x}^3)$, so that the line element (ds) is written as $(ds)^2 = -(c\hat{d}\hat{t})^2 + \sum_{i=1}^3 (d\hat{x}^i)^2$.

The basic equations in the 3+1 formalism are written as

$$\frac{\partial D}{\partial t} = -\frac{1}{h_1 h_2 h_3} \sum_{i=1}^3 \frac{\partial}{\partial x^i} \left[\frac{\alpha h_1 h_2 h_3}{h_i} D (\hat{v}^i + c\beta^i) \right], \quad (11)$$

$$\begin{aligned} \frac{\partial \hat{P}^i}{\partial t} &= -\frac{1}{h_1 h_2 h_3} \sum_{j=1}^3 \frac{\partial}{\partial x^j} \left[\frac{\alpha h_1 h_2 h_3}{h_j} (\hat{\tau}^{ij} + c\beta^j \hat{P}^i) \right] \\ &\quad - (\epsilon + Dc^2) \frac{1}{h_j} \frac{\partial \alpha}{\partial x^i} + \alpha f_{\text{curve}}^i - \sum_{j=1}^3 \hat{P}^j \sigma_{ji}, \end{aligned} \quad (12)$$

$$\frac{\partial \epsilon}{\partial t} = -\frac{1}{h_1 h_2 h_3} \sum_{i=1}^3 \frac{\partial}{\partial x^i} \left[\frac{\alpha h_1 h_2 h_3}{h_i} c^2 \left(\hat{P}^i - D \hat{v}^i + \frac{\beta^i}{c} \epsilon \right) \right] - \sum_{i=1}^3 c^2 \hat{P}^i \frac{1}{h_i} \frac{\partial \alpha}{\partial x^i} - \sum_{i,j} \hat{T}^{ij} \sigma_{ji}, \quad (13)$$

where $f_{\text{curve}}^i \equiv \sum_{j=1}^3 (G_{ij} \hat{T}^{ij} - G_{ji} \hat{T}^{ji})$, $G_{ij} \equiv -(1/h_i h_j)(\partial h_i / \partial x^j)$, and $\sigma_{ij} \equiv (h_i / h_j)(\partial \omega_i / \partial x^j)$. Moreover D , \hat{P}^i , \hat{T}^{ij} , and ϵ are the mass density, energy flux density, momentum flux density, and energy density corrected by rest-mass energy in the FIDO frame, respectively. They are represented as

$$D = \gamma \rho, \quad (14)$$

$$\hat{P}^i = \frac{1}{c^2} H \gamma^2 \hat{v}^i, \quad (15)$$

$$\hat{T}^{ij} = p \delta^{ij} + \frac{H}{c^2} \gamma^2 \hat{v}^i \hat{v}^j, \quad (16)$$

$$\epsilon = H \gamma^2 - p - D c^2, \quad (17)$$

where $\gamma = 1/[1 + \sum_{i=1}^3 (d\hat{x}^i/c dt)^2]^{1/2}$, $H = \rho c^2 + \Gamma p / (\Gamma - 1) = (e_{\text{int}} + p)$, and δ^{ij} are the Lorentz factor, the specific relativistic enthalpy, and Kronecker's δ -symbol, respectively. Hereafter a hat over a quantity denotes that it is evaluated in the FIDO frame.

2.3. Numerical Method

We have used a simplified total variation diminishing method, which was developed by Davis (1984) for violent phenomena such as shock waves. This method is qualitatively similar to the Lax-Wendroff method with a diffusion term. In order to integrate the time-dependent conservation laws, we have to calculate neither eigenvectors nor eigenvalues of the coefficient matrix of the linearized GRHD equations. The only procedure necessary is to calculate the maximum speed of the waves.

During the time evolution of the differential equations, we obtain the quantities D , \hat{P} , and ϵ at each time step directly. In order to proceed to the next time step, we have to calculate γ , \hat{v} , and p from the conserved quantities D , \hat{P} , and ϵ . Therefore, we must solve the nonlinear algebraic equation

$$X(X+2)(\Gamma R X + \Gamma R - d)^2 = (\Gamma X^2 + 2\Gamma X + 1)^2 f^2, \quad (18)$$

where $X \equiv \gamma - 1$, $R = D + \epsilon/c^2$, $d = (\Gamma - 1)D$, and $f = \hat{P}/c$. This equation is the same as that derived by Duncan & Hughes (1994). The equation is solved at each mesh point by using the Newton-Raphson iteration method. Thus, we can easily obtain \hat{v} and p from X , ρ , D , \hat{P} , and ϵ .

2.4. Parameters

There are four parameters in our problem:

$$\frac{\rho_d}{\rho_c} \equiv \frac{\text{proper mass density of the accretion disk}}{\text{proper mass density of the corona}}, \quad (19)$$

$$\frac{\hat{v}_\phi}{\hat{V}_K} \equiv \frac{\text{azimuthal velocity of the accretion disk}}{\text{Keplerian velocity}}, \quad (20)$$

$$a \equiv \frac{J}{J_{\text{max}}} = \frac{J}{M r_g c} = \frac{c^2 J}{GM^2} = \text{spin parameter of the black hole}, \quad (21)$$

$$E_{\text{th}} \equiv \frac{\text{thermal energy}}{\text{gravitational energy}} = \frac{C_s^2}{\hat{V}_K^2}, \quad (22)$$

where $C_s [\equiv c(\Gamma p/H)^{1/2}]$ and \hat{V}_K represent the proper sound speed and the Keplerian velocity, respectively. The Keplerian velocity is written as

$$\hat{V}_K = c \frac{A}{\Delta^{1/2} (r^3 - r_g^3 a^2)} \left[\pm \sqrt{\frac{r_g}{r}} - a \left(\frac{r_g}{r} \right)^2 \right] - c \frac{h_3 \omega_3}{c\alpha}, \quad (23)$$

where the positive and negative signs correspond to orbits that corotate and counterrotate, respectively, with the black hole. In our simulations, only corotating cases are treated. Under a Schwarzschild metric, $\hat{V}_K = c/[2(r/r_S - 1)]^{1/2}$.

2.5. Initial and Boundary Conditions

Initial conditions are as follows: In the $a = 0.0$ case, we assume that the region between $x = 3.0r_S$ and $40.0r_S$ (the outer boundary) is filled with an accretion disk. On the other hand, in the $a = 0.99$ case, there is an accretion disk in the region between $x = 0.73r_S$ and $40.0r_S$. In both cases the inner edge of the disk is determined from the marginally stable orbit. The azimuthal velocity of the disk is taken to be a sub-Keplerian velocity ($\hat{v}_\phi/\hat{V}_K = 0.95$) in both cases. If the disk is rotating at the Keplerian velocity, it is steady and never falls to the black hole without viscosity. On the other hand, if the disk rotation is sub-Keplerian, the disk falls in a dynamical timescale, which gives a finite-amplitude disturbance to the disk. We put the disk corona in the region between the inner boundary of the simulation area and the inner edge of the disk. The distributions of the proper mass density, proper pressure, and radial velocity in the FIDO frame in the corona are determined from the Bondi solution. This is not the exact Bondi solution, but the radial velocity in the FIDO frame near the black hole is always supersonic in both cases. Hence, the information cannot be transported from the black hole to the simulation area. The proper mass density in the disk is taken as $\rho_d/\rho_c = 1000$ ($a = 0.0$) and $\rho_d/\rho_c = 100$ ($a = 0.99$). The proper pressure in the disk is determined to be balanced with the coronal pressure. Hence, the ratio of the temperature distribution in the disk to that of the corona is 0.001 ($a = 0.0$) and 0.01 ($a = 0.99$). The distribution of E_{th} is not uniform, where E_{th} at the inner edge of the disk is taken as $E_{\text{th}} = 0.024$ ($a = 0.0$) and $E_{\text{th}} = 0.13$ ($a = 0.99$).

As for boundary conditions, the inner and outer boundaries in the radial direction are assumed to be free boundaries, so that the differentiation of physical variables at the boundaries does not change with time. This condition means that waves and fluids can pass through each boundary freely.

3. RESULTS

From the results of the simulations, we obtained quasi-periodic inward shock waves. First we show the snapshots of physical quantities in the $a = 0.0$ case (Fig. 3). Figure 3a shows the initial conditions. There is an accretion disk in the region between $x = 3.0r_S$ and $40.0r_S$ rotating at a sub-Keplerian velocity ($\hat{v}_\phi/\hat{V}_K = 0.95$). After the disk falls to the black hole, it becomes a Keplerian disk at $t = 67\tau_S$ ($\tau_S \equiv r_S/c$), as seen in Figure 3b. In Figure 3c we can see an inwardly propagating shock front at $x = 2.6r_S$. After this time, the shock wave propagates toward the black hole, and other inward shock waves are generated and propagate quasi-periodically toward the black hole.

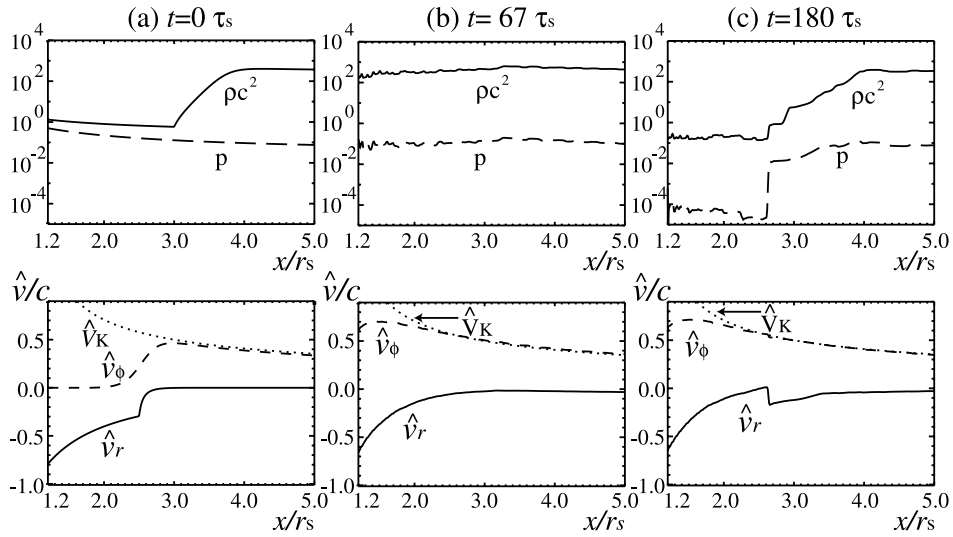


FIG. 3.—Snapshots of the spatial distribution of physical quantities in the $a = 0.0$ case. The horizontal axis shows the distance from the black hole in units of r_s . The physical quantities are at (a) $t = 0\tau_s$ ($\tau_s \equiv r_s/c$), (b) $67\tau_s$, and (c) $180\tau_s$. In the top panels, the solid and dashed curves show the proper mass density (ρ) and proper pressure (p) (on a logarithmic scale), respectively. In the bottom panels, the solid, dashed, and dotted curves show the radial velocity (\hat{v}_r), the azimuthal velocity (\hat{v}_ϕ), and the Keplerian velocity (\hat{V}_K) in the FIDO frame in units of light speed on a linear scale, respectively. In (a) the disk, from $x = 3.0r_s$ to $40.0r_s$, is rotating at sub-Keplerian velocity initially: $\hat{v}_\phi/\hat{V}_K = 0.95$. In (b) we can see that the azimuthal velocity in the FIDO frame becomes the Keplerian velocity through the supply of angular momentum from the outer to the inner region of the disk. In (c), at about $t = 180\tau_s$ an inward shock wave is formed, and the shock front can be seen at $x = 2.6r_s$.

To get an overview of the propagation of shock waves, we show the time evolution of the proper pressure in Figure 4. We can see that the inward shock waves are generated and propagate from the disk toward the black hole quasi-periodically.

Figure 5 shows the time variation of the proper pressure at $x = 2.5r_s$. The passage of shock waves can be seen. The strong shock waves are generated quasi-periodically with a

period of $\simeq 149\tau_s$. The rotation period at the inner edge of the disk ($x = 3.0r_s$) is $\simeq 46.2\tau_s$ for comparison.

In Figure 6 we show the normalized power spectral density (PSD) of the radial velocity \hat{v}_r at $x = 2.5r_s$. A characteristic feature can be seen at $6.70 \times 10^{-3}\tau_s^{-1}$, which corresponds to a frequency of $\sim (149\tau_s)^{-1}$. Moreover, several higher harmonics can also be seen.

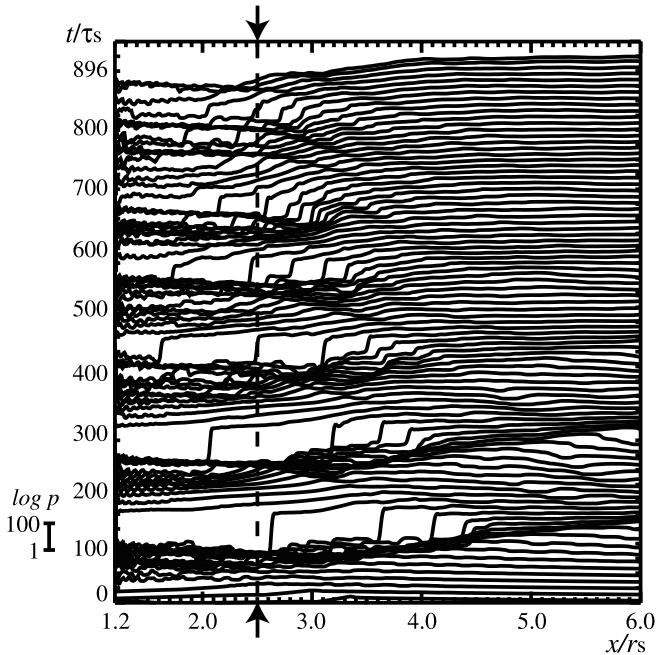


FIG. 4.—Detailed time evolution of the propagation of shock waves in the $a = 0.0$ (Schwarzschild black hole) case. Proper pressures are plotted as a function of the distance from the black hole in units of r_s (on a logarithmic scale), stacked with time increasing upward uniformly by $10\tau_s$. Several inward shock waves and many wavy structures are generated and propagate toward the black hole. The distribution of proper pressure along the arrows and dashed line is shown in Fig. 5.

Proper pressure ($x=2.5r_s$)

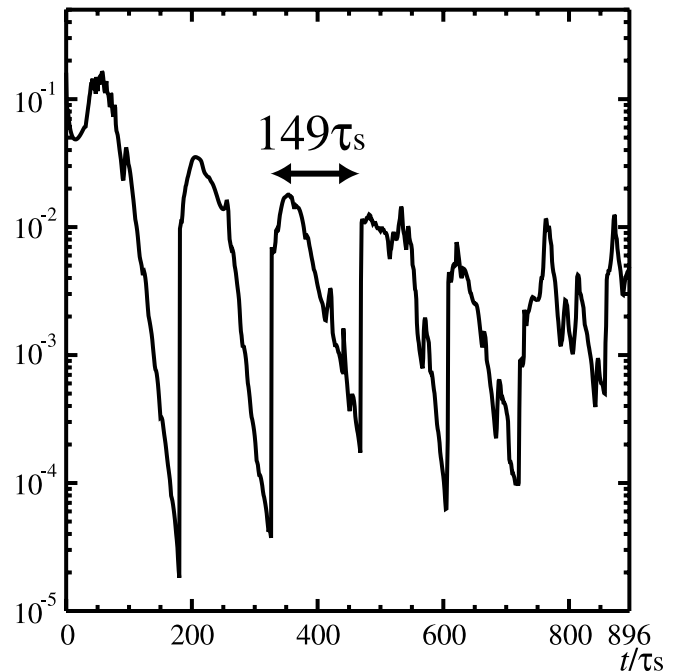


FIG. 5.—Time variation of the proper pressure at $x = 2.5r_s$ in the $a = 0.0$ case. The horizontal axis shows time in units of τ_s on a linear scale, whereas the vertical axis shows the proper pressure on a logarithmic scale. This figure shows the distribution along the arrows and dashed line in Fig. 4. The characteristic period of passage of large shock waves is $\sim 149\tau_s$, and numerous small variations can be seen.

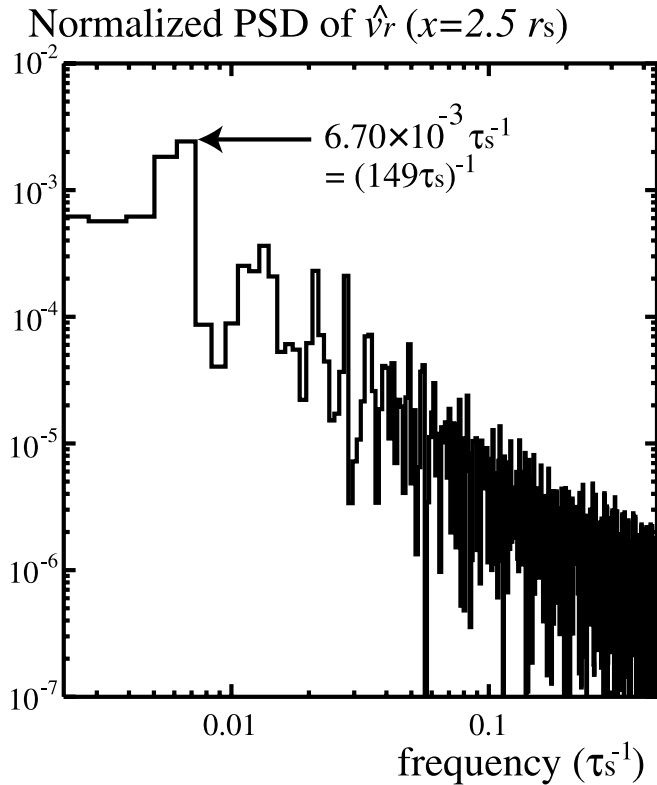


FIG. 6.—Normalized PSD of the radial velocity \hat{v}_r in the FIDO frame at $x = 2.5r_S$ in the $a = 0.0$ case. The horizontal axis shows the frequency in units of τ_S^{-1} on a logarithmic scale, whereas the vertical axis shows on a logarithmic scale the PSD of the radial velocity in the FIDO frame at $x = 2.5r_S$, normalized by total power. There is a characteristic frequency at $\sim 6.70 \times 10^{-3} \tau_S^{-1}$, which corresponds to a period of $\sim (149\tau_S)^{-1}$ (see Fig. 5). Several of its higher harmonics can also be seen. The bin width of the frequency is $1.12 \times 10^{-3} \tau_S^{-1}$.

Next we discuss the results in the $a = 0.99$ case. Figure 7 shows the snapshots of physical variables. The initial conditions are shown in Figure 7a. The region between $x = 0.73r_S$ and $40r_S$ is occupied by the accretion disk, and the azimuthal velocity of the disk is taken to be $\hat{v}_\phi = 0.95\hat{V}_K$. The disk becomes Keplerian in Figure 7b. Figure 7c shows the inwardly propagating shock front at $x \simeq 0.88r_S$. Several shock waves are generated and propagate toward the black hole quasi-periodically after this time.

In order to get an overview of the quasi-periodic generation and propagation of inward shock waves, we show the time evolution of the proper pressure in Figure 8. The inward shock waves are generated and propagate toward the black hole quasi-periodically.

Figure 9 shows the time variation of the proper pressure at $x = 0.65r_S$. The period of passage of the shock waves is $\simeq 44\tau_S$. The rotation period of the disk at the inner edge of the disk ($x = 0.73r_S$) is $\simeq 5.5\tau_S$ for comparison.

From the normalized PSD of \hat{v}_r at $x = 0.65r_S$ (Fig. 10), we can see that there are many characteristic frequencies. The lowest frequency is $2.26 \times 10^{-2} \tau_S^{-1}$, which corresponds to a frequency of $\sim (44\tau_S)^{-1}$. Its higher harmonics can also be seen.

In order to confirm that the characteristic frequency does not depend on the parameter \hat{v}_ϕ/\hat{V}_K , we performed the simulations in other sub-Keplerian cases such as $\hat{v}_\phi = (0.75, 0.85, 0.9)\hat{V}_K$ for both $a = 0.0$ and $a = 0.99$. In all cases, the characteristic frequencies are not different from that of the $\hat{v}_\phi/\hat{V}_K = 0.95$ case. We confirm that no shock wave is generated in the Keplerian case ($\hat{v}_\phi/\hat{V}_K = 1.0$) for $a = 0.0$ and 0.99 .

For $\hat{v}_\phi/\hat{V}_K = 0.65, 0.75, \text{ and } 0.85$, another type of shock wave is also generated in addition to the quasi-periodic inward shock waves. This type of shock wave is generated only once and propagates outward. In the $\hat{v}_\phi/\hat{V}_K = 0.95$ case, this wave cannot be clearly seen because accretion flow is weak. The outward shock wave is caused by the effects of the centrifugal force, and the physical mechanism driving the shock is the

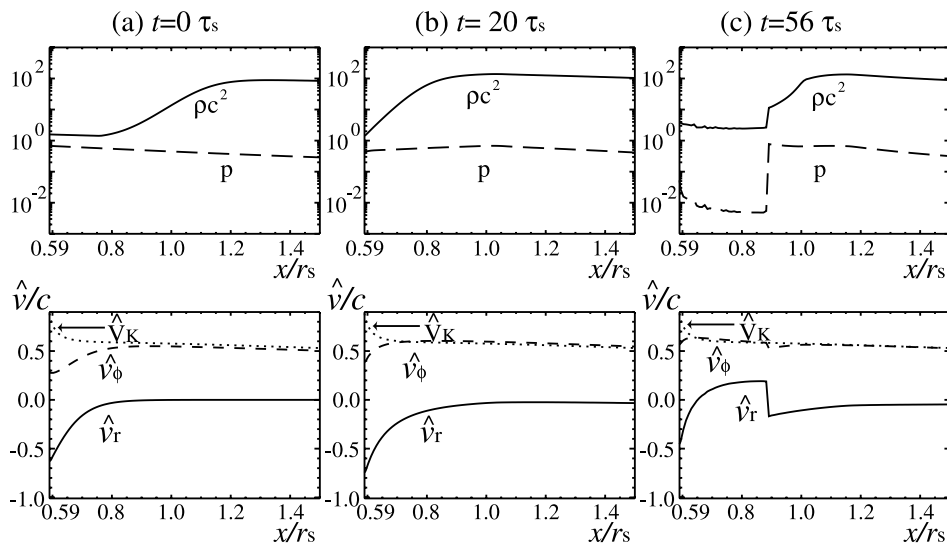


FIG. 7.—Snapshots of the spatial distribution of the physical quantities of the $a = 0.99$ (rapidly rotating Kerr black hole) case. The horizontal axis shows the distance from the black hole in units of r_S . The physical quantities are at (a) $t = 0\tau_S$, (b) $20\tau_S$, and (c) $56\tau_S$. In the top panels, the solid and dashed curves show proper mass density (ρ) and proper pressure (p) (on a logarithmic scale), respectively. In the bottom panels, the solid, dashed, and dotted curves show the radial velocity (\hat{v}_r), the azimuthal velocity (\hat{v}_ϕ), and the Keplerian velocity (\hat{V}_K) in the FIDO frame in units of the speed of light on a linear scale, respectively. In (a) the disk, from $x = 0.73r_S$ to $40.0r_S$, is rotating at sub-Keplerian velocity initially: $\hat{v}_\phi/\hat{V}_K = 0.95$. In (b) the azimuthal velocity in the FIDO frame becomes the Keplerian velocity through the supply of angular momentum from the outer to the inner region of the disk. In (c), at about $t = 56\tau_S$ an inward shock wave is formed, and the shock front can be seen at $x = 0.88r_S$.

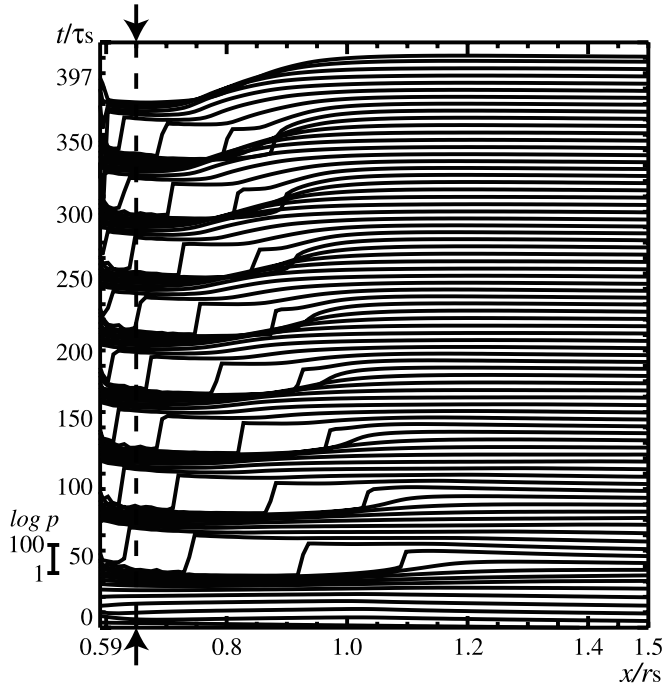


FIG. 8.—Detailed time evolution of the propagation of shock waves in the $a = 0.99$ case. The proper pressures are plotted as a function of the distance from the black hole in units of r_S (on a logarithmic scale), stacked with time uniformly increasing upward by $5\tau_S$. Several inward shock waves are generated and propagate toward the black hole. The distribution of the proper pressure along the arrows and dashed line is shown in Fig. 9.

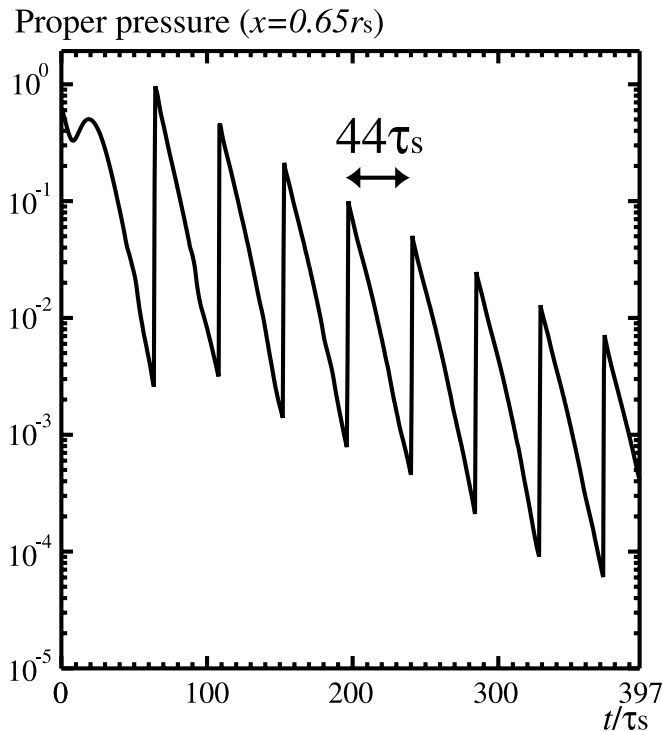


FIG. 9.—Time variation of the proper pressure at $x = 0.65r_S$ in the $a = 0.99$ case. The horizontal axis shows time in units of τ_S on a linear scale, whereas the vertical axis shows the proper pressure on a logarithmic scale. This is the distribution along the arrows and dashed line in Fig. 8. The characteristic period of the passage of shock waves is $\sim 44\tau_S$.

Normalized PSD of \hat{v}_r ($x=0.65 r_S$)

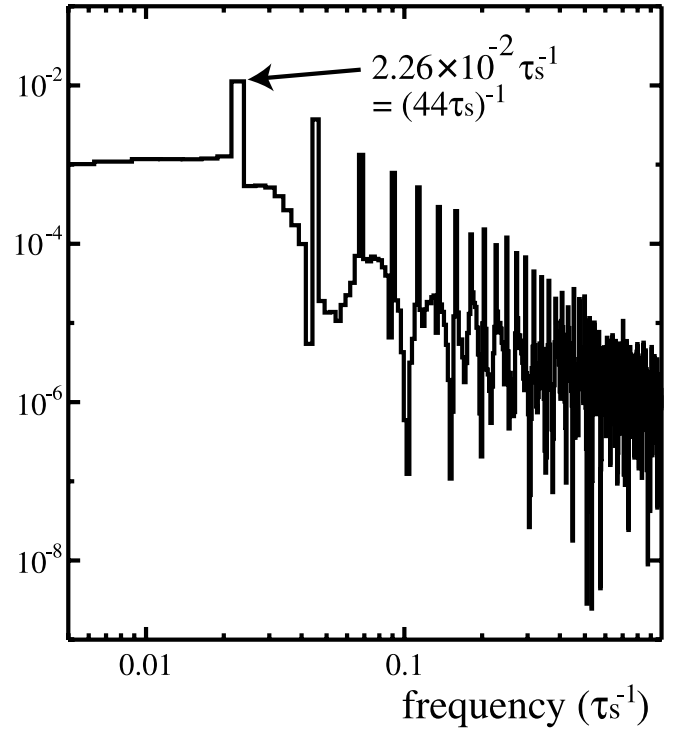


FIG. 10.—Normalized PSD of the radial velocity \hat{v}_r in the FIDO frame at $x = 0.65r_S$ in the $a = 0.99$ case. The horizontal axis shows frequency in units of τ_S^{-1} on a logarithmic scale, whereas the vertical axis shows on a logarithmic scale the PSD of the radial velocity in the FIDO frame at $x = 0.65r_S$, normalized by total power. The characteristic feature can be seen at $2.26 \times 10^{-2} \tau_S^{-1}$. We can also see several of its higher harmonics. The lowest frequency of the harmonics is comparable to $(44\tau_S)^{-1}$ (see Fig. 9). The bin width of the frequency is $2.51 \times 10^{-3} \tau_S^{-1}$.

same as that producing the shock accelerating the gas pressure driven jet (Koide et al. 1998, 1999, 2000).

4. DISCUSSION

The lowest characteristic frequency for each spin parameter is $\sim \kappa_{\max}/2\pi$ (κ_{\max} is the maximum epicyclic frequency in the disk), which depends on the rotation of the black hole. Before discussing the mechanism of the production of the quasi-periodic inward shock waves, we explain the epicyclic frequency.

4.1. Epicyclic Frequency

The radial oscillation of orbital motion is known as epicyclic motion, which occurs when a radial perturbation is given to a point mass rotating around a massive object in a circular orbit. The epicyclic frequency (κ) distribution in an accretion disk around a rotating black hole as a function of radius (x) is given as (Okazaki et al. 1987)

$$\kappa = \Omega \frac{\sqrt{1 - 3r_S/x + 8a(r_S/2x)^{3/2} - 3a^2(r_S/2x)^2}}{1 + a(r_S/2x)^{3/2}}, \quad (24)$$

where $\Omega [= (GM/x^3)^{1/2}]$ is the Keplerian angular frequency around a Schwarzschild black hole. In the $a = 0.0$

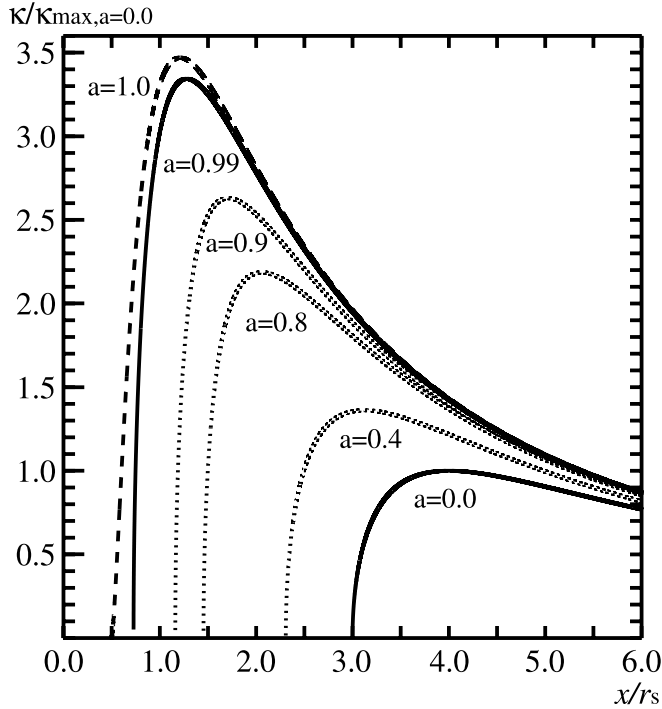


FIG. 11.—Dependence of the epicyclic frequency on a , the spin parameter of the black hole. In this figure, only $a \geq 0$ (corotating) cases, which means that the direction of the rotation of the accretion disk is the same as that of the black hole, are shown. The horizontal axis shows the distance from the black hole in units of r_s , whereas the vertical axis shows the frequency of the waves in units of the maximum epicyclic frequency in the $a = 0.0$ case. In the nonrotating black hole case ($a = 0.0$; lower solid curve), there is a maximum epicyclic frequency at $x = 4.0r_s$. The larger a is, the higher the maximum epicyclic frequency becomes. When $a = 0.99$ (upper solid curve), the maximum epicyclic frequency is ~ 3.34 times that in the $a = 0.0$ case, and the radius where epicyclic frequency becomes the maximum is $x \simeq 1.28r_s$. The $a = 1.0$ case (dashed curve) is also shown, and the maximum epicyclic frequency is ~ 3.47 times that in the $a = 0.0$ case.

(Schwarzschild black hole) case, κ is simplified as $\kappa = (1 - 3r_g/x)^{1/2}\Omega$. The dependence of κ on the spin parameter of the black hole, a , is shown in Figure 11. The larger the spin parameter of the black hole is, the higher the maximum value of κ becomes. In the nonrelativistic limit, κ is equal to the Keplerian angular frequency, and there is no finite maximum value in the κ -distribution.

4.2. Shock Formation Mechanisms

In order to investigate the formation mechanism of quasi-periodic inward shock waves, we studied the wave propagation when a linear perturbation is injected into an accretion disk, and then compared it with quasi-periodic inward shock formation.

4.2.1. Linear Perturbation Case

We discuss the wave propagation in the disk from the point of view of the dispersion relation of acoustic waves to see how the wave propagation is induced by the disturbances. When we assume axial symmetry and one-dimensional propagation in the equatorial plane of the accretion disk around a rotating black hole, the dispersion relation is written as

$$\omega^2 = \kappa^2 + k^2 V_s^2, \quad (25)$$

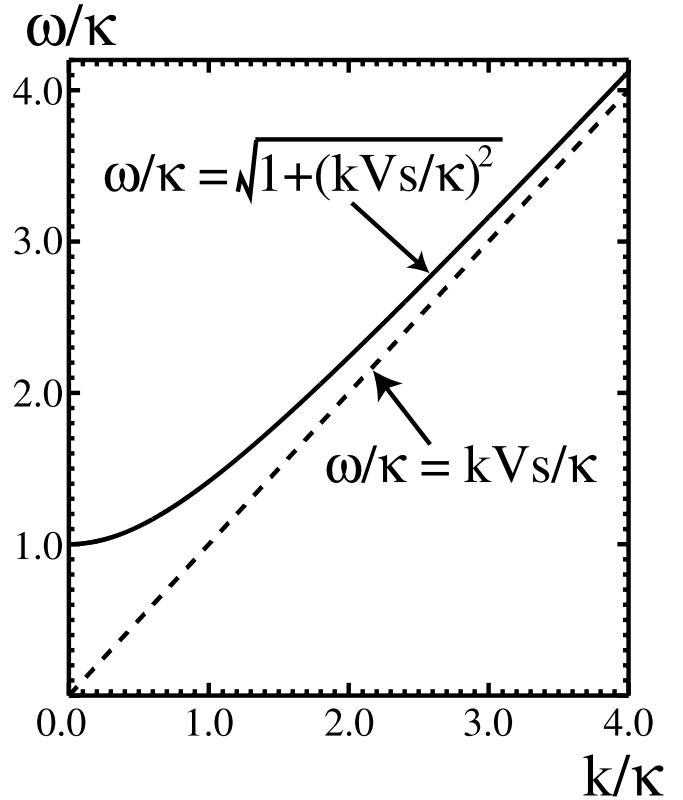


FIG. 12.—Dispersion relation of acoustic waves in an accretion disk, where ω , k , κ , and V_s indicate the frequency of induced waves, the wavenumber of perturbation, the epicyclic frequency in the disk, and the speed related to the sound speed, respectively. The solid curve represents the dispersion relation $\omega/\kappa = [1 + (kV_s/\kappa)^2]^{1/2}$. The slope of the curve of the dispersion relation is the group velocity. Hence, the lower ω/κ becomes, the smaller the group velocity of the induced wave is. Therefore, the group velocity of the induced wave with frequency κ is equal to zero. The minimum frequency of ω is κ . Waves with frequency lower than κ are forbidden. The dashed line shows the asymptotic line of the dispersion relation in the limit of $k/\kappa \rightarrow \infty$, and the slope of the line gives the maximum group velocity, which is equal to V_s .

where ω and k are the frequency of the induced wave and the wavenumber of the perturbation, respectively, and V_s is the effective speed and is related to the sound speed by

$$V_s^2 = C_s^2 \frac{h_0^2 + (h_3\omega_3/c)^2}{h_1^2 \left[1 + \sum_{i=1}^3 (\hat{v}^i/c)^2 \right]} \times \left[1 - \left(\frac{C_s}{c} \right)^2 \frac{(h_3\omega_3/c - h_3\Omega/c)^2}{(h_3\omega_3/c)^2 - h_0^2} \right]^{-1}. \quad (26)$$

The derivation of the dispersion relation (25) is given in Appendix A. Figure 12 shows the dispersion relation at a fixed point in the disk. The slope of the solid curve gives the group velocity, and the maximum group velocity is equal to V_s . The larger the wavenumber k of the perturbation is, the faster the group velocity of the induced wave becomes. The minimum frequency of the induced wave is κ , and its group velocity is equal to zero. Therefore, when the frequency of the wave is almost equal to κ , the propagation speed of the wave is very small, and the time necessary for the waves to propagate is the longest among the permitted waves. Hence, when various modes are injected by the perturbation, the wave with frequency $\sim \kappa$ becomes dominant with time. This behavior

is similar to that of vertical acoustic wave propagation in the atmosphere (wake), which has been discussed by Lamb (1932; see also Suematsu et al. 1982; Kalkofen et al. 1994).

In order to show that the quasi-periodic inward shock formation can be explained by analysis based on linear theory, we performed another simulation with a linear perturbation. We call this simulation the “linear perturbation case.” On the other hand, we call the simulations shown in § 3 the “sub-Keplerian case.” The difference in the initial conditions in the linear perturbation case from those in the sub-Keplerian case are as follows: (1) there are 9000 mesh points in the region between $x = 3.1r_S$ and $40.0r_S$ with uniform mesh sizes; (2) the simulation region is filled only by an accretion disk; (3) the proper mass density and proper pressure are assumed to be constant in the simulation region, values of which are determined so that the proper sound speed is equal to that at $x = 4.0r_S$ in the sub-Keplerian case: $C_s = 0.18c$; (4) the accretion disk is rotating at the Keplerian velocity ($\hat{v}_\phi/\hat{V}_K = 1.0$); (5) the black hole is not rotating ($a = 0.0$); (6) a perturbation is injected into the radial velocity of 1% of the proper sound speed in the FIDO frame at $x = 7.1r_S$ (only one mesh point), which induces various wave modes. The position of the perturbation injection is determined so that the induced waves propagate through the point of κ_{\max} ($x = 4.0r_S$) toward the inner region of the disk. In the linear perturbation case, only small perturbations are injected in a steady state disk. Hence, the physical quantities of the disk such as proper mass density, proper pressure, and rotation of the disk do not vary largely with time.

Figure 13 shows the time variation of the radial velocity \hat{v}_r at $x = 7.1r_S$ in the linear perturbation case. The solid curve indicates the result of the simulation, whereas the dashed curve shows the analytic solution derived from linear theory. The result from the simulation is in very good agreement with the analytic solution. The deviation of the result of the simulation from that of the analytic solution after $t \sim 400\tau_S$ is due to the mixing with reflected waves at the inner boundary of the simulation area. Here we show the explicit form of the analytic solution. When the perturbation is injected into the radial velocity at one point in the form of a delta function, the time variation of the radial velocity \hat{v}_r , derived from linear analysis is written as (see Appendix A)

$$\hat{v}_r(x, t) = -\frac{F_0}{2} \frac{t}{\sqrt{t^2 - [(x - x_0)/V_s(x_0)]^2}} \times J_1 \left(\kappa(x_0) \sqrt{t^2 - \left[\frac{x - x_0}{V_s(x_0)} \right]^2} \right), \quad (27)$$

where x_0 , F_0 , and J_1 represent the position where the perturbation is injected, the normalization factor of \hat{v}_r , and the Bessel function, respectively; $V_s(x_0)$ and $\kappa(x_0)$ are the effective speed and epicyclic frequency at $x = x_0$, respectively. Here this analytic solution can be applied only in the region where $\kappa(x)$ and $V_s(x)$ are not very different from those at the point of the perturbation injection $[\kappa(x_0), V_s(x_0)]$. The time variation of \hat{v}_r shown in Figure 13 is obtained by setting $x = x_0$ in equation (27):

$$\hat{v}_r(x_0, t) = -\frac{F_0}{2} J_1(\kappa(x_0)t). \quad (28)$$

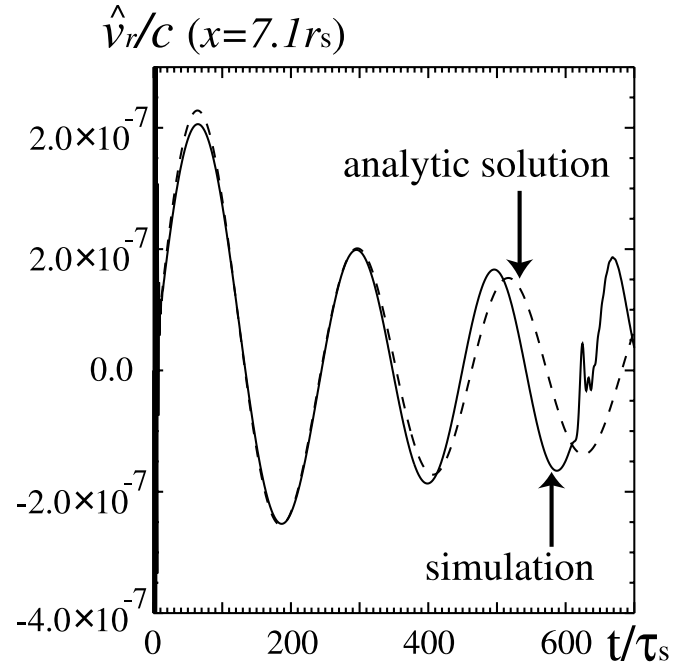


FIG. 13.—Comparison of the time variation of the radial velocity in the FIDO frame from the simulation in the linear perturbation case with that from the analytic solution. The horizontal axis shows time in units of τ_S , whereas the vertical axis shows the velocity in units of the speed of light. The time variation of the radial velocity in the FIDO frame at the point of the perturbation injection ($x = 7.1r_S$) is shown by the solid curve. The dashed curve shows the analytic solution (eq. [28]). Hence, the result of the simulation is in good agreement with that from the analytic solution. The deviation of the simulation result from that of the analytic solution after $t \sim 400\tau_S$ is due to mixing with the reflected waves at the inner boundary of the simulation area ($x = 3.1r_S$).

We can see from equation (28) that the time variation of \hat{v}_r at the point of the perturbation injection is determined by $\kappa(x_0)$.

In fact, from the normalized PSD of \hat{v}_r observed in the simulation, the characteristic frequency in the PSD at the point of the perturbation injection is $\sim 5.07 \times 10^{-3} \tau_S^{-1}$ [denoted by (1) in Fig. 14]. This frequency is almost equal to $\kappa/2\pi$ at $x = 7.1r_S$: $4.49 \times 10^{-3} \tau_S^{-1}$ (the characteristic frequency is larger than $\kappa/2\pi$ at $x = 7.1r_S$ by 1.8%, taking into account the error due to the bin width in the normalized PSD), which is predicted from the linear theory as we mentioned above. The factor 2π in $\kappa/2\pi$ is the normalization factor of the frequency in the PSD. After the perturbation injection, the induced waves propagate toward the inner region of the disk and reach $x = 4.0r_S$, where κ becomes the maximum value (κ_{\max}). The characteristic frequency in the PSD at $x = 4.0r_S$ [denoted by (2) in Fig. 14] becomes $\sim 8.13 \times 10^{-3} \tau_S^{-1}$. This frequency is nearly equal to $\kappa_{\max}/2\pi$: $7.03 \times 10^{-3} \tau_S^{-1}$ (the characteristic frequency is larger than $\kappa_{\max}/2\pi$ by 8.3%, taking into account the error due to the bin width in the normalized PSD). Then, the induced waves reach the inner region of the disk ($x = 3.2r_S$). Although $\kappa/2\pi$ at $x = 3.2r_S$ is $\sim 4.90 \times 10^{-3} \tau_S^{-1}$, the characteristic frequency in the PSD at this point [denoted by (3) in Fig. 14] is the same as that at $x = 4.0r_S$. Hence, the characteristic frequency in the PSD is much higher than $\kappa/2\pi$ at $x = 3.2r_S$. Here we note that the waves with frequency lower than κ_{\max} are cut off.

Therefore, the nonuniform finite distribution of κ in the disk acts as a filter. That is, if the frequency of a wave is lower than κ_{\max} , the wave can reach neither the inner region of the disk nor the vicinity of the black hole. Hence, we can explain in Figure 15

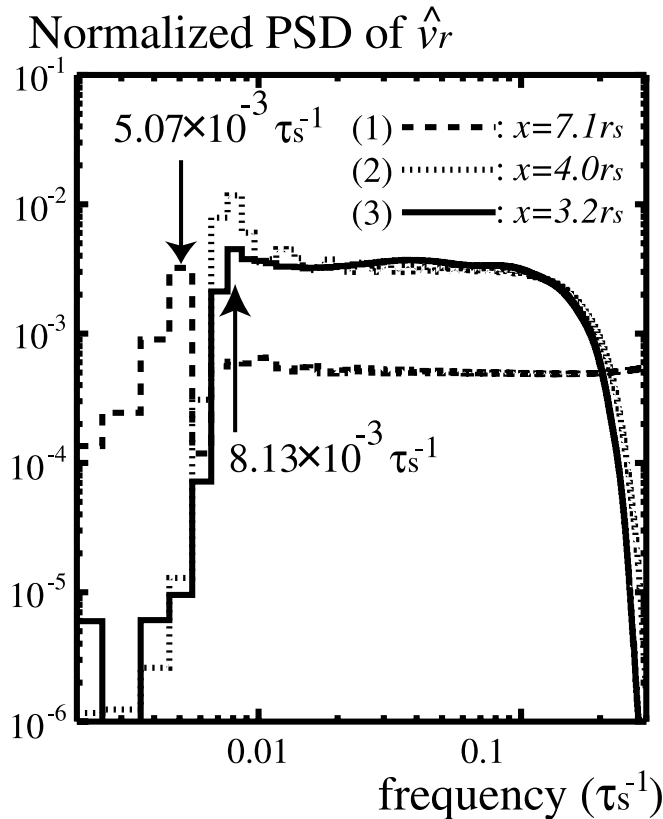


FIG. 14.—Normalized PSD of the radial velocity in the FIDO frame at several fixed points in the linear perturbation case. The horizontal axis shows the frequency in units of τ_S^{-1} on a logarithmic scale, whereas the vertical axis shows on a logarithmic scale the PSD of the radial velocity in the FIDO frame, normalized by the total power. The dashed, dotted, and solid curves represent the normalized PSD of the radial velocity in the FIDO frame at $x = 7.1r_S$, $4.0r_S$, and $3.2r_S$, respectively. The perturbation is injected at $x = 7.1r_S$ initially. The characteristic frequency at $x = 7.1r_S$ is $\sim 5.07 \times 10^{-3} \tau_S^{-1}$. This is almost equal to $\kappa/2\pi$ at this point. The induced waves propagate toward $x = 4.0r_S$, where κ becomes κ_{\max} . The characteristic frequency at $x = 4.0r_S$ is $\sim 8.13 \times 10^{-3} \tau_S^{-1}$, nearly equal to $\kappa/2\pi$ here. Then the induced waves go through to the inner region of the disk ($x = 3.2r_S$), where $\kappa/2\pi$ is $\sim 4.90 \times 10^{-3} \tau_S^{-1}$. However the characteristic frequency at this point is the same as that at $x = 4.0r_S$ ($\kappa_{\max}/2\pi$) and much higher than $\kappa/2\pi$ at $x = 3.2r_S$. The waves with frequencies lower than κ_{\max} are cut off.

the wave propagation in the system of a Schwarzschild black hole and an accretion disk. In this figure, the solid curve denotes κ in the disk in the $a = 0.0$ (Schwarzschild black hole) case, whereas the dashed curve represents κ in the nonrelativistic limit. The lowest frequency of the wave induced by perturbations becomes κ from the dispersion relation (see Fig. 12). Hence, a wave induced in the region outside the radius where κ becomes κ_{\max} in the disk can propagate toward the black hole when its frequency is larger than κ_{\max} . Moreover, among the induced waves a wave with frequency $\sim \kappa_{\max}$ becomes dominant in both the inner region of the disk and the vicinity of the black hole, which is explained by the dispersion relation. Therefore, a coherent wave is produced near the black hole by this filtering effect on the wave propagation. The frequency of the coherent wave becomes $\sim \kappa_{\max}$. In the nonrelativistic limit, κ becomes infinite near a central object, and no wave with a finite frequency can reach the central object.

4.2.2. Sub-Keplerian Case

We showed why the frequency of the oscillation in the vicinity of the black hole becomes $\sim \kappa_{\max}$ in the linear pertur-

bation case. Figure 16 shows the comparison of the time variation of the radial velocity \hat{v}_r at a fixed point in the linear perturbation case with that in the sub-Keplerian case. We can see that the global shape of the time variation of \hat{v}_r in the linear perturbation case is similar to that in the sub-Keplerian case. The period of the time variation of \hat{v}_r at $x = 3.4r_S$ in the linear perturbation case is $\sim 131\tau_S$, which is near the period $2\pi/\kappa_{\max}$: $142\tau_S$. (It is slightly smaller than the period $2\pi/\kappa_{\max}$ by 7.7%.) As for the sub-Keplerian case, the period of the time variation of \hat{v}_r at $x = 3.4r_S$ is $\sim 149\tau_S$. It is within the error range of the period $2\pi/\kappa_{\max}$. Therefore, both the period of the oscillation in the linear perturbation case and that of the quasi-periodic inward shock formation in the sub-Keplerian case are near the period $2\pi/\kappa_{\max}$ in the disk.

In the sub-Keplerian case, the initial disturbance is injected everywhere in the disk, whereas in the linear perturbation case the initial perturbation is injected only at one point. Hence, the sub-Keplerian case can be regarded as the superposition of linear perturbation cases whose perturbations are injected everywhere in the disk. As we discussed above, the characteristic period of the oscillation in the vicinity of the black hole in the linear perturbation case becomes $\sim 2\pi/\kappa_{\max}$ because of the filtering effect by the nonuniform finite epicyclic frequency distribution in the disk. In the sub-Keplerian case, the initial disturbances are injected not only in the outer region of the disk but also in the inner region of the disk. However, the effect of the induced waves in the region between the inner edge of the disk and the radius where κ becomes κ_{\max} is probably small, because this region is very narrow relative to the outer region of the disk. Therefore, the induced waves in the inner region of the disk would not affect the characteristic period in the sub-Keplerian case. In fact, the characteristic period at $x = 2.5r_S$ in the sub-Keplerian case becomes the period $\sim 2\pi/\kappa_{\max}$ in spite of the fact that the region is interior to the radius where κ becomes κ_{\max} . Hence, in the sub-Keplerian case, the period of the quasi-periodic inward shock formation is also determined by the filtering effect due to the nonuniform finite epicyclic frequency distribution.

The initial disturbance in the sub-Keplerian case is very large, so that the amplitude of induced waves becomes large and nonlinear effects become important. The physical conditions near the black hole also affect the shock formation. Material near a black hole is swallowed into the hole. Therefore, the proper mass density becomes smaller in the vicinity of the black hole. The energy flux of an acoustic wave is approximately conserved during its propagation toward the black hole, so that the velocity amplitude of a wave becomes large when the wave comes into the low-density region near the black hole. If the velocity amplitude exceeds the proper sound speed, nonlinear effects become important, and waves evolve to shock waves.

Consequently, we conclude that the period of the quasi-periodic inward shock formation is also determined by the filtering effect due to the nonuniform finite epicyclic frequency distribution in the sub-Keplerian case. The differences of amplitude and detailed shape between the linear perturbation case and the sub-Keplerian case are due to the superposition and nonlinear effects.

As for the $a = 0.99$ case, the characteristic frequency of the quasi-periodic inward shock formation is $\sim 2.26 \times 10^{-2} \tau_S^{-1}$. This frequency is within the error range of the frequency κ_{\max} : $2.35 \times 10^{-2} \tau_S^{-1}$. Hence, in the $a = 0.99$ case the frequency of the quasi-periodic inward shock formation also becomes $\sim \kappa_{\max}/2\pi$. To confirm this behavior, we have examined the cases of $a = 0.90$ and $a = 0.95$. The characteristic frequency

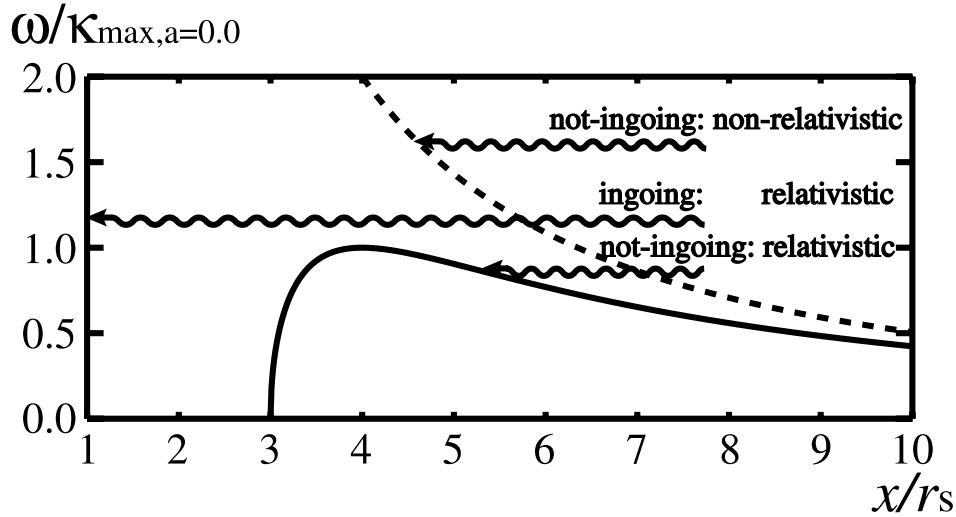


FIG. 15.—Wave propagation in the system of a Schwarzschild black hole and an accretion disk. The horizontal axis shows the distance from the black hole in units of r_s on a linear scale, whereas the vertical axis shows the frequency of waves (ω) in units of the maximum epicyclic frequency in the disk of the Schwarzschild black hole case ($\kappa_{\max, a=0.0}$) on a linear scale; the epicyclic frequency (κ) becomes a maximum value at $x = 4.0r_s$. The solid curve indicates the epicyclic frequency in the disk in the general relativistic treatment. On the other hand, the dotted curve indicates that in the nonrelativistic limit, which is equal to the Keplerian angular frequency. The wavy arrows show the wave propagation. From the dispersion relation (see Fig. 12), acoustic waves with frequencies higher than a maximum epicyclic frequency (κ_{\max}) can reach the black hole; on the other hand, waves with frequencies lower than κ_{\max} cannot reach the black hole. Hence, the lower limit of the frequency of the waves that can reach the black hole is determined by κ_{\max} . In the nonrelativistic limit, κ becomes infinite near the central object, so that no wave can reach the central object. When the black hole is corotating ($a > 0.0$), κ is larger than that in the $a = 0.0$ case (see Fig. 11). Therefore, the lower limit of the frequency of the waves that can reach the black hole in the $a > 0.0$ case becomes larger than that in the $a = 0.0$ case.

of the quasi-periodic inward shock formation in the $a = 0.90$ case is $1.99 \times 10^{-2} \tau_s^{-1}$. This is within the error range of $\kappa_{\max}/2\pi$ in the $a = 0.90$ case: $1.84 \times 10^{-2} \tau_s^{-1}$. As for the $a = 0.95$ case, the characteristic frequency of the quasi-periodic inward shock formation is $1.94 \times 10^{-2} \tau_s^{-1}$. This is also within the error range of $\kappa_{\max}/2\pi$ in the $a = 0.95$ case: $2.08 \times 10^{-2} \tau_s^{-1}$. Therefore, the characteristic frequency of the quasi-

periodic inward shock formation can be explained by the filtering effect of the nonuniform finite epicyclic frequency distribution in the disk. The frequency of the shock formation becomes $\sim \kappa_{\max}/2\pi$ in the disk around a Kerr black hole.

The results of our simulations are not caused by wave trapping, which is predicted by linear theory in the disk-oscillation model (Kato & Fukue 1980; Kato 1989, 1990, 2001; Nowak et al. 1997; Perez et al. 1997; Kato et al. 1998; Nowak & Lehr 1998; Wagoner 1999). In our result, the coherent waves or quasi-periodic inward shock waves are produced by the filtering effect due to the nonuniform distribution of the epicyclic frequency in the disk. We do not need the viscosity in the disk, which was essential to exciting oscillations in previous numerical simulations, such as the ones by Matsumoto et al. (1988, 1989), Honma et al. (1992), and Chen & Taam (1995) in one dimension and Milsom & Taam (1997) in two dimensions. The only necessary condition is a non-steady character for the disk. Such turbulent disks are indeed predicted by magnetohydrodynamic (MHD) simulations as a result of the magnetorotational instability in accretion disks in two dimensions (Balbus & Hawley 1991, 1992; Hawley & Balbus 1991, 1992; Tagger et al. 1992; Tout & Pringle 1992; Vishniac & Diamond 1992; Stone & Norman 1994; Matsumoto et al. 1996) and in three dimensions (Brandenburg et al. 1995; Hawley et al. 1995; Matsumoto & Tajima 1995; Stone et al. 1996; Matsumoto 1999; Hawley 2000; Machida et al. 2000; Machida & Matsumoto 2003).

In our simulations, the amplitude of the quasi-periodic inward shock waves decreases with time. In order to have long-lasting quasi-periodic inward shock formation, we must set the condition of the sub-Keplerian rotation into the disk repeatedly. This condition can be attained by intermittent mass accretion, which has been found in the 2.5-dimensional resistive MHD simulations of astrophysical jets by Kuwabara et al. (2000). They showed that mass accretion and jet formation occur intermittently because of the magnetorotational

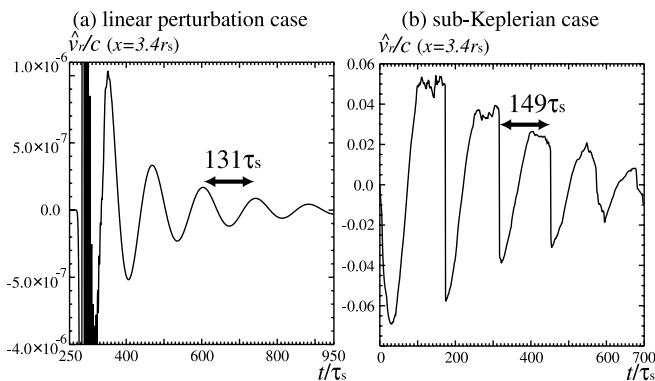


FIG. 16.—Comparison of the time variation of the radial velocity in the FIDO frame at a fixed point from (a) the linear perturbation case with that from (b) the sub-Keplerian case. In each panel the horizontal axis and vertical axis indicate the time in units of τ_s and the radial velocity in the FIDO frame at $x = 3.4r_s$ in units of the speed of light, respectively. The same time ranges are shown in both panels. In (a) the initial perturbation is very small and given at only one mesh point, whereas in (b) the initial perturbation is very large and given everywhere in the disk. Therefore, the result from the sub-Keplerian case is due to the superposition of the large perturbations everywhere in the disk, which causes nonlinear effects to become important. The frequency of the dominant waves near the inner edge of the disk is $\sim \kappa_{\max}$, as discussed previously. This implies in both the linear perturbation case and the sub-Keplerian case that the period of the oscillation of the dominant wave becomes $\sim 142\tau_s$ ($= 2\pi/\kappa_{\max}$). In the sub-Keplerian case, the characteristic period of the oscillation ($149\tau_s$) is within the error range of the period $2\pi/\kappa_{\max}$. In the linear perturbation case, it is also similar ($131\tau_s$) to the period $2\pi/\kappa_{\max}$; to be exact, the characteristic frequency is slightly smaller than the period $2\pi/\kappa_{\max}$ by 7.7%.

instability in the disk when the resistivity is taken to be small.

Recently, a QPO with frequency $\sim \kappa_{\max}$ was found in three-dimensional MHD simulations of an accretion disk with a pseudo-Newtonian potential (Machida & Matsumoto 2003). It is probable that the mechanism of their oscillation is similar to our mechanism for quasi-periodic inward shock formation, because the distribution of the azimuthal velocity of the disk in our initial conditions is very similar to that in their simulations when the oscillations occur.

4.3. Comparisons with the High-Frequency QPOs in Microquasars

QPOs are believed to originate from the central regions of black hole objects and are possibly associated with shock formation there. When we assume the typical mass of a BHC in a microquasar to be $M_{\text{BHC}} \sim 10 M_{\odot}$, the frequency of the quasi-periodic inward shock formation ($\kappa_{\max}/2\pi$) around a nonrotating black hole ($a = 0.0$) is estimated to be ~ 71 Hz, and that around a maximally rotating black hole ($a = 1.0$) becomes ~ 248 Hz. Therefore, they are on the order of the frequencies in high-frequency QPOs in microquasars: ~ 100 Hz. Hence, the high-frequency QPOs in microquasars can be explained by the frequency of the quasi-periodic inward shock formation. Moreover, κ_{\max} depends on the spin of the black hole, so that we can estimate the spin of the BHC in microquasars by comparing the frequency of high-frequency QPOs with κ_{\max} .

Figure 17 shows the dependence of $\kappa_{\max}/2\pi$ on the spin parameter of the black hole and a comparison of it with the frequency of high-frequency (ν) QPOs in microquasars, GRS 1915+105 and GRO J1655–40. It can be seen that κ_{\max} is within the error range of the frequency of the inward shock formation for each spin parameter. We use $\nu(M_{\text{BH}}/M_{\odot})$ for the vertical axis in Figure 17, because κ_{\max} is in inverse proportion to the mass of the black hole. Because κ_{\max} largely depends on the spin parameter of the black hole, we can estimate the spin parameter of a BHC in a microquasar by comparing $\kappa_{\max}/2\pi$ with the frequency of high-frequency QPOs. In addition, we can estimate the spin parameter of a BHC in a microquasar if the mass of the BHC is determined quite precisely from observations, for example, of GRS 1915+105 and GRO J1655–40. The high-frequency QPOs in GRS 1915+105 show double peaks at 40 and 67 Hz (Morgan et al. 1997; Strohmayer 2001b), and the mass of the central BHC is estimated as $14 \pm 4 M_{\odot}$ by Greiner et al. (2001). The error range of the spin parameter of a BHC in a microquasar is determined by both the accuracy of the estimation of the BHC's mass from observations and that of the frequency of the quasi-periodic inward shock formation for each spin parameter in our simulations. The error of the spin parameter due to the accuracy of the mass estimation of the BHC is a few times larger than that of the frequency of the shock formation. Here we assume the error of the frequency of the shock formation to be 9% of the frequency, which is the maximum value in our simulations. The ranges of $\nu(M_{\text{BH}}/M_{\odot})$ of the high-frequency QPOs in GRS 1915+105 estimated from these errors are shown in Figure 17 for two frequencies, (1) 40 Hz and (2) 67 Hz. We cannot know which of the frequencies, 40 or 67 Hz, corresponds to $\kappa_{\max}/2\pi$. If we suppose that the 40 Hz component corresponds to $\kappa_{\max}/2\pi$, the BHC is almost not rotating ($a = 0.08 \pm 0.08$). On the other hand, the spin parameter of the black hole is estimated to be $a = 0.345 \pm 0.345$ if we assume the 67 Hz component corresponds to $\kappa_{\max}/2\pi$. The high-frequency QPOs in GRO

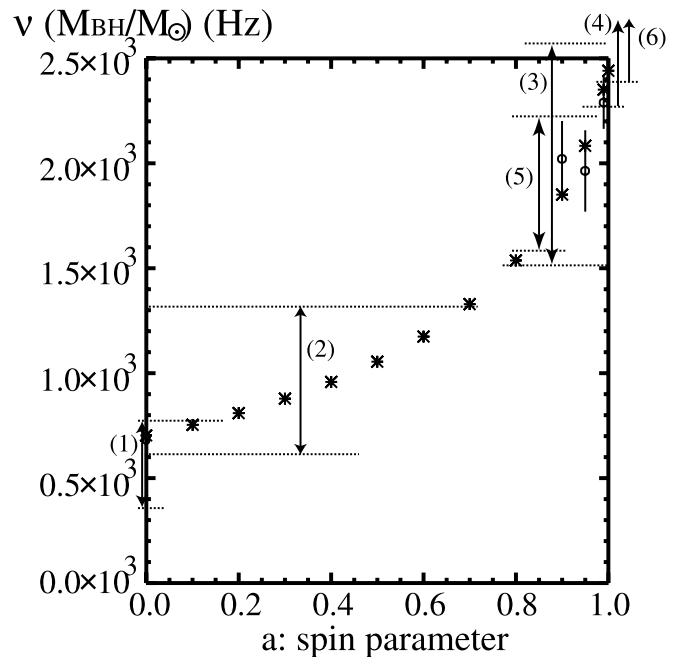


FIG. 17.—Comparison of the maximum epicyclic frequency with high-frequency QPOs in microquasars. The horizontal axis shows the spin parameter of the black hole, a , on a linear scale, whereas the vertical axis shows the frequency on a logarithmic scale. The asterisks indicate $\kappa_{\max}/2\pi$, which is obtained from eq. (24). The open circles with bars represent the frequencies of the quasi-periodic inward shock formation in our simulations with error ranges. The high-frequency QPOs, assuming the mass of the BHC in GRS 1915+105 estimated by Greiner et al. (2001) including the error of the frequency of the quasi-periodic inward shock formation in our simulations, are indicated for (1) the 40 Hz and (2) the 67 Hz components. For GRO J1655–40, they are indicated for (3) the 300 Hz and (4) the 450 Hz components, assuming the mass of the BHC estimated by Shahbaz et al. (1999). Moreover, they are indicated for (5) the 300 Hz and (6) the 450 Hz components, assuming the mass of the BHC estimated by Greiner et al. (2001). The spin parameter of the BHC can be estimated for (1) the 40 Hz and (2) the 67 Hz components in GRS 1915+105 as $a = 0.08 \pm 0.08$ and 0.345 ± 0.345 , respectively. For GRO J1655–40, the spin parameter of the BHC for (3) the 300 Hz and (4) the 450 Hz components can be estimated to be $a = 0.895 \pm 0.105$ and 0.99 ± 0.01 , respectively, assuming the mass of the BHC by Shahbaz et al. (1999). If we assume the mass of the BHC by Greiner et al. (2001), the spin parameter of the BHC can be estimated as $a = 0.885 \pm 0.075$ for (5) the 300 Hz and $a = 0.995 \pm 0.005$ for (6) the 450 Hz component.

J1655–40 also show double peaks at 300 and 450 Hz (Remillard et al. 1999b; Strohmayer 2001a), and the mass of the central BHC is determined as $5.5\text{--}7.9 M_{\odot}$ by Shahbaz et al. (1999) or $6.3 \pm 0.5 M_{\odot}$ by Greiner et al. (2001). If we assume the mass of the BHC by Greiner et al. (2001), the spin parameter of the BHC can be estimated to be (3) $a = 0.895 \pm 0.105$ for the 300 Hz component and (4) $a = 0.99 \pm 0.01$ for the 450 Hz component. When we use the mass of the BHC by Greiner et al. (2001), the spin parameter of the BHC can be estimated to be (5) $a = 0.885 \pm 0.075$ for the 300 Hz component and (6) $a = 0.995 \pm 0.005$ for the 450 Hz component.

4.4. Future Problems

The high-frequency QPOs in GRS 1915+105 and GRO J1655–40 show double peaks; one peak is not a harmonic of the other peak. However, in our result only one fundamental mode and its higher harmonics were seen. On the basis of the disk-oscillation model, various types of oscillations such as inertial acoustic waves (p -modes), inertial gravity waves

(g -modes), and corrugation waves can occur. The p -mode is an oscillation in the radial direction, whereas the g -mode is in the direction perpendicular to the equatorial plane of the disk. The corrugation waves are generated by the coupling of these two modes. Our simulations were performed in 1.5-dimensional coordinates, so that only the p -mode could be seen. This is the reason that we could not reproduce the double peaks of the high-frequency QPOs in GRS 1915+105 and GRO J1655–40. The double peaks could be due to the mixing of various wave modes. Therefore, they could be reproduced by two-dimensional or three-dimensional (magneto-) hydrodynamic simulations.

It is known that observed high-frequency QPOs show broad peaks in the power spectra of their light curves, which are evaluated with the coherence parameter $Q = \nu_0/\delta\nu_{\text{FWHM}}$ (ν_0 : central frequency of the peak of the QPO; $\delta\nu_{\text{FWHM}}$: width of the peak). In our simulations, the values $Q_{\text{sim}} \equiv \nu/\nu_{\text{bw}}$ (ν : a frequency of the peak in the PSD; ν_{bw} : bin width of the peak) correspond to the coherence parameters. Those in the $a = 0.0, 0.90, 0.95,$ and 0.99 cases are comparable to the coherence parameters of the frequencies of the high-frequency QPOs in GRS 1915+105 and GRO J1655–40. Hence, the frequency resolutions in the PSDs are not high enough to discuss the broadness of the peaks in the power spectra. In order to discuss this, longer term simulations are necessary.

One X-ray nova, XTE J1550–564, shows time-variable high-frequency QPOs (Remillard et al. 1999a; Homan et al. 2001), and its central black hole mass is quite precisely estimated by Orosz et al. (2002). These highly time variable QPOs cannot be explained by our model. In order to explain this behavior, a more complicated model is necessary.

5. SUMMARY

We have performed 1.5-dimensional general relativistic hydrodynamic simulations to propose a model of high-frequency QPOs in microquasars. The simulations were performed for the equatorial plane of an accretion disk without disk viscosity around a Kerr black hole. In order to induce acoustic waves, we assumed that the disk was initially rotating at 0.95 times the Keplerian velocity instead of including viscosity in the disk. We call these simulations the “sub-Keplerian cases.” We performed the simulations for spin parameters of the black hole of $a = 0.0, 0.90, 0.95,$ and 0.99 . It was found that quasi-periodic shock waves propagate toward the black hole. The frequencies of the shock formation are $\sim 6.70 \times 10^{-3} \tau_S^{-1}$ ($a = 0.0$), $\sim 1.99 \times 10^{-2} \tau_S^{-1}$ ($a = 0.90$), $\sim 1.94 \times 10^{-2} \tau_S^{-1}$ ($a = 0.95$), and $\sim 2.26 \times 10^{-2} \tau_S^{-1}$ ($a = 0.99$), respectively. Each frequency is about the maximum epicyclic frequency in the accretion disk ($\kappa_{\text{max}}/2\pi$), which depends on the spin parameter of the black hole.

In order to investigate the mechanism of the quasi-periodic inward shock formation, we performed another simulation with a linear perturbation, which can be understood by linear theory. We call this simulation the “linear perturbation case.” In the linear perturbation case, we inject an initial perturbation into the radial velocity of 1% of the proper sound speed in the FIDO frame at one mesh point in the Keplerian disk. This perturbation induces various acoustic wave modes. From linear theory, the lowest frequency of the induced waves is the epicyclic frequency (κ), and the wave with frequency $\sim \kappa$ becomes dominant with time among the induced waves. In fact, the time variation of the radial velocity in the FIDO frame at the point of the perturbation injection in the linear perturbation case is in good agreement with that of

the analytic solution derived in linear theory. The distribution of κ in an accretion disk is not uniform, and its maximum value is finite under a general relativistic treatment. Hence, if the frequency of the acoustic wave induced at the outer region of the disk is higher than κ_{max} , the wave can reach the vicinity of the black hole. Moreover, the lowest frequency of the waves that can reach the black hole is κ_{max} , so that the wave with frequency $\sim \kappa_{\text{max}}$ becomes dominant with time near the black hole. Therefore, the nonuniform epicyclic frequency distribution in the disk acts as a filter on the wave propagation toward the black hole in the linear perturbation case.

The sub-Keplerian case can be regarded as the superposition of linear perturbation cases everywhere in the disk. The amplitudes of the induced waves in the sub-Keplerian case are very large, because the initial perturbation is very strong. Hence, nonlinear effects become important. In addition, the proper mass density is very low near the black hole, so that the induced waves evolve to shocks propagating toward the black hole. Therefore, the characteristic frequency of the quasi-periodic inward shock formation is also determined by the filtering effect due to the nonuniform finite epicyclic frequency distribution. Consequently, the quasi-periodic inward shock formation is not due to wave trapping, which is predicted by linear theory in the disk-oscillation model. The only necessary condition for shock formation in our result is the nonsteady character of the disk. Such turbulent disks are indeed predicted by MHD simulations as a result of the magnetorotational instability in accretion disks. In three-dimensional MHD simulations of accretion disks with a pseudo-Newtonian potential, it has been found that a QPO with κ_{max} occurs (Machida & Matsumoto 2003). Although our model is very simple, the mechanism that produces quasi-periodic inward shock waves may be the same as that which produces the radial oscillations described in the work of Machida & Matsumoto (2003).

The frequency of the quasi-periodic inward shock formation is $\sim \kappa_{\text{max}}/2\pi$ and on the order of the frequencies in high-frequency QPOs in microquasars. Therefore, we think that high-frequency QPOs in microquasars can be explained by quasi-periodic inward shock formation. Hence, we can estimate the spin parameter of a BHC in a microquasar by comparing $\sim \kappa_{\text{max}}/2\pi$ with the frequency of high-frequency QPOs. The value κ_{max} largely depends on the mass, so we have chosen microquasars whose BHC masses are quite precisely determined from observations, i.e., GRS 1915+105 and GRO J1655–40. From our model, taking the 40 and 67 Hz components in GRS 1915+105, we predict the spin parameter of the BHC to be $a = 0.08 \pm 0.08$ and 0.345 ± 0.345 , respectively. As for GRO J1655–40, there are two estimations of the BHC mass by Shahbaz et al. (1999) and Greene et al. (2001). In the case of Shahbaz et al. (1999), the spin parameter of the BHC for the 300 and 450 Hz components is estimated to be $a = 0.895 \pm 0.105$ and 0.99 ± 0.01 , respectively. On the other hand, in the Greene et al. (2001) case, we suggest that the spin parameter of the BHC for the 300 and 450 Hz components is $a = 0.885 \pm 0.075$ and 0.995 ± 0.005 , respectively.

The high-frequency QPOs in GRS 1915+105 and GRO J1655–40 show double peaks, although in our result only one mode can be seen. On the basis of the disk-oscillation model, several types of waves are induced, such as inertial acoustic waves (p -mode), inertial gravity waves (g -mode), and corrugation waves. The p -mode is an oscillation in the radial direction, which is obtained in our 1.5-dimensional simulations.

In order to reproduce the double high-frequency QPOs, two-dimensional or three-dimensional general relativistic (magneto-) hydrodynamic simulations are probably necessary.

We would like to thank S. Kato for useful comments and discussions. We also thank T. Haugbølle for helpful comments. This work is supported by the Japan Science and Technology Corporation (ACT-JST), the Japan Society for the

Promotion of Science Japan-UK Cooperation Science Program (principal investigators: K. Shibata and N. O. Weiss), and a grant-in-aid for the 21st Century Center of Excellence ‘‘Center for Diversity and Universality in Physics.’’ The numerical computations were carried out on VPP5000 at the Astronomical Data Analysis Center of the National Astronomical Observatory, Japan, which is an interuniversity research institute of astronomy operated by the Ministry of Education, Culture, Sports, Science, and Technology.

APPENDIX A

LINEAR PERTURBATION ANALYSIS

In this paper we deal with radially one-dimensional perturbations in accretion disks. If the perturbations are restricted to being infinitesimal, adiabatic, and local, their propagation characteristics are properly captured by the dispersion relation (25) or its corresponding wave equation,

$$\frac{\partial^2 \hat{v}_r}{\partial t^2} + \kappa^2 \hat{v}_r - V_s^2 \frac{\partial^2 \hat{v}_r}{\partial r^2} = 0. \quad (\text{A1})$$

In this appendix we derive equation (A1) and its solution in equation (27).

Equation (A1) can be obtained by a conventional recipe; linearize basic equations (1) and (2), eliminate variables other than \hat{v}_r , and apply the local approximation in order to remove some terms including the radial gradient of the unperturbed quantities. In the following, we enter into details about this process.

For the purpose of deriving equation (A1), it is useful to rewrite the energy-momentum conservation equation (2) in the form of the Euler equation:

$$L_{\tilde{U}} \tilde{U} = -(\tilde{d} + \tilde{U}L_{\tilde{U}}) \int \frac{C_s^2(\rho)}{\rho} d\rho, \quad (\text{A2})$$

where L is the Lie derivative, \tilde{d} is the exterior derivative, $\tilde{U} = U^\nu \tilde{\partial}_\nu$, and $\tilde{U} = U_\nu \tilde{d}x^\nu$. The right-hand side should primarily be $-(\tilde{d} + \tilde{U}L_{\tilde{U}})p/(e_{\text{int}} + p)$. In the present case, however, we deal with an adiabatic gas; any thermodynamic quantity depends, therefore, only on one independent variable, i.e., ρ . Thus, we have $\delta p/(e_{\text{int}} + p) = \delta \int [C_s^2(\rho)/\rho] d\rho$. Note that the Euler equation (A2) gives the equation of force balance in the radial direction for the equilibrium state:

$$-\frac{1}{U_0^t} \frac{dU_0^t}{dr} + \frac{l}{1 - l\Omega} \frac{d\Omega}{dr} = -\frac{C_s^2}{\rho_0} \frac{d\rho_0}{dr}, \quad (\text{A3})$$

where $\Omega \equiv U_0^\phi/U_0^t$ and $l \equiv -U_{\phi 0}/U_{t 0}$ are the angular velocity and the specific angular momentum, respectively. This equation is tacitly used in our following derivation.

Next, we decompose each physical quantity into an equilibrium component and an infinitesimal, radial perturbation as $\tilde{U} = \tilde{U}_0(r) + \tilde{U}_1(t, r)$, $\tilde{U} = \tilde{U}_0(r) + \tilde{U}_1(t, r)$, and $\rho = \rho_0(r) + \rho_1(t, r)$ and linearize the basic equations (1) and (A2). The continuity equation (1) is linearized as

$$U_0^t \frac{\partial \rho_1}{\partial t} + \rho_0 l \frac{\partial U_1^\phi}{\partial t} + \frac{1}{\sqrt{-g}} \frac{\partial(\sqrt{-g} \rho_0 U_1^r)}{\partial r} = 0. \quad (\text{A4})$$

Although the Euler equation (A2) and hence also its linearization consist of three nontrivial component equations, only two of them are independent; we decompose equation (A2) into $\tilde{d}r$, $\tilde{d}\phi$, and $(\tilde{d}t - l\tilde{d}\phi)$ components and write linearized equations for the first two:

$$g_{rr} U_0^t \frac{\partial U_1^r}{\partial t} + \left[(g_{t\phi} l + g_{\phi\phi}) U_0^t \frac{d\Omega}{dr} + U_{t0} \frac{dl}{dr} \right] U_1^\phi = -\frac{\partial}{\partial r} \left(C_s^2 \frac{\rho_1}{\rho_0} \right), \quad (\text{A5})$$

$$(1 - l\Omega) (g_{t\phi} l + g_{\phi\phi}) U_0^t \frac{\partial U_1^\phi}{\partial t} - U_{t0} \frac{dl}{dr} U_1^r = -l \frac{\partial}{\partial t} \left(C_s^2 \frac{\rho_1}{\rho_0} \right). \quad (\text{A6})$$

In deriving the above equations (A4)–(A6), we have used the subsidiary relations $U_{t1} = -\Omega U_{\phi 1} = -\Omega (g_{t\phi} l + g_{\phi\phi}) U_1^\phi$ and $U_1^t = l U_1^\phi$, which are given by the linearization of the normalization condition $U^\nu U_\nu = -1$.

Eliminating variables other than

$$U_1^r = \left(1 - \frac{2r_g r}{\Sigma} + \frac{A\omega_3^2}{\Sigma c^2} \right)^{1/2} \left(\frac{\Delta}{\Sigma} \right)^{1/2} \frac{U_0^t \hat{v}^r}{c} \equiv N U_0^t \hat{v}^r$$

from equations (A4)–(A6), we obtain

$$\left(\frac{\partial^2}{\partial t^2} + \kappa^2\right)\hat{v}_r = V_s^2 \left(\frac{\partial}{\partial r} + Q\right) \left(\frac{\partial}{\partial r} + P\right)\hat{v}_r, \quad (\text{A7})$$

where

$$P \equiv \frac{d}{dr} \log[\sqrt{-g}\rho_0 U_0^t N] + \frac{U_{t0} l}{U_0^t (1 - l\Omega)(g_{t\phi} l + g_{\phi\phi})} \frac{dl}{dr}, \quad (\text{A8})$$

$$Q \equiv \frac{d}{dr} \log[g_{rr} N V_s^2 (U_0^t)^2] - \frac{l}{1 - l\Omega} \left[\frac{d\Omega}{dr} + \frac{U_{t0}}{(g_{t\phi} l + g_{\phi\phi}) U_0^t} \frac{dl}{dr} \right]. \quad (\text{A9})$$

The epicyclic frequency on the equatorial plane, κ , is given by expression (24) for a Keplerian disk around a Kerr black hole. More generally, it is defined by

$$\kappa^2 \equiv \frac{U_{t0}}{g_{rr}(1 - l\Omega)U_0^t} \frac{dl}{dr} \left[\frac{d\Omega}{dr} + \frac{U_{t0}}{(g_{t\phi} l + g_{\phi\phi})U_0^t} \frac{dl}{dr} \right]. \quad (\text{A10})$$

In addition, in terms of the present notation, the effective sound speed V_s , which is given by equation (26), is defined by

$$\begin{aligned} V_s^2 &\equiv \frac{C_s^2}{g_{rr}(U_0^t)^2} \left[1 - \left(\frac{C_s}{c}\right)^2 \frac{(g_{\phi t} + \Omega g_{\phi\phi})^2}{g_{t\phi}^2 - g_{tt}g_{\phi\phi}} \right]^{-1} \\ &= C_s^2 \frac{h_0^2 + (h_3\omega_3/c)^2}{h_1^2 \left[1 + \sum_{i=1}^3 (\hat{v}^i/c)^2 \right]} \left[1 - \left(\frac{C_s}{c}\right)^2 \frac{(h_3\omega_3/c - h_3\Omega/c)^2}{(h_3\omega_3/c)^2 - h_0^2} \right]^{-1}. \end{aligned} \quad (\text{A11})$$

Equation (A7) shows that the wave propagation characteristics are governed by the restoring effects of the centrifugal force (the second term including κ on the left-hand side) and the compressibility (the right-hand side term including V_s), although the latter is modified by the spatial inhomogeneity of the equilibrium state as expressed by P and Q , consisting of radial gradient terms of the equilibrium quantities. We are, however, restricted to the case in which the local approximation is applicable. This approximation assumes that the spatial variation scale of the perturbations should be much less than that of the equilibrium quantities. Therefore, it allows us to treat the background equilibrium state as homogeneous. Thus, P and Q are removed from the right-hand side, and only $V_s^2 \partial^2 \hat{v}_r / \partial r^2$ remains as the dominant term expressing the effects of compressibility. We are thus led to equation (A1).

Finally, we derive expression (27) for the radial velocity perturbation \hat{v}_r . It is a solution of equation (A1) satisfying the initial conditions

$$\hat{v}_r(x, 0) = F_0 \delta(x - x_0), \quad \frac{\partial \hat{v}_r}{\partial t}(x, 0) = 0, \quad (\text{A12})$$

where x_0 is the position of the perturbation injection.

To derive the solution in equation (27), we Fourier transform \hat{v}_r as

$$\hat{v}_r(x, t) = \int_{-\infty}^{\infty} w(k, t) \exp(ik(x - x_0)) dk. \quad (\text{A13})$$

(Note that, according to the local approximation, we regard κ and V_s as constant.) Then, $w(k, t)$ obeys the second-order differential equation

$$\frac{\partial^2 w}{\partial t^2} + (k^2 V_s^2 + \kappa^2)w = 0, \quad (\text{A14})$$

the general solution of which is expressed as

$$w(k, t) = A(k) \cos\left(t\sqrt{k^2 V_s^2 + \kappa^2}\right) + B(k) \sin\left(t\sqrt{k^2 V_s^2 + \kappa^2}\right). \quad (\text{A15})$$

The coefficients $A(k)$ and $B(k)$ are determined by the initial condition (A12) as $A(k) = F_0$ and $B(k) = 0$. We thus obtain our solution in equation (27) as

$$\hat{v}_r(x, t) = \frac{F_0}{2\pi} \int_{-\infty}^{\infty} \cos\left[t\sqrt{k^2 V_s^2(x_0) + \kappa(x_0)^2}\right] \exp[ik(x - x_0)] dk$$

$$= \begin{cases} \frac{F_0}{2} \frac{J_1\left(\kappa(x_0)t\sqrt{1 - [(x - x_0)/V_s(x_0)t]^2}\right)}{\sqrt{1 - [(x - x_0)/V_s(x_0)t]^2}}, & t \geq \frac{|x - x_0|}{V_s(x_0)}, \\ 0, & 0 \leq t < \frac{|x - x_0|}{V_s(x_0)}, \end{cases} \quad (\text{A16})$$

where $\kappa(x_0)$ and $V_s(x_0)$ are the values of κ and V_s at $x = x_0$, respectively.

REFERENCES

- Alpar, A., & Shaham, J. 1985, *Nature*, 316, 239
 Balbus, S. A., & Hawley, J. F. 1991, *ApJ*, 376, 214
 ———. 1992, *ApJ*, 400, 610
 Beardmore, A. P., & Osborne, J. P. 1997, *MNRAS*, 286, 77
 Boyer, R. H., & Lindquist, R. W. 1967, *J. Math. Phys.*, 8, 265
 Brandenburg, A., Nordlund, Å., Stein, R. F., & Torkelsson, U. 1995, *ApJ*, 446, 741
 Chen, X., & Taam, R. E. 1995, *ApJ*, 441, 354
 Cui, W., Zhang, S. N., & Chen, W. 1998, *ApJ*, 492, L53
 Cui, W., Zhang, S. N., Chen, W., & Morgan, E. H. 1999, *ApJ*, 512, L43
 Davis, S. F. 1984, NASA Contractor Rep. 172373 (ICASE Rep 84-20; Washington, DC: NASA)
 Duncan, G. C., & Hughes, P. A. 1994, *ApJ*, 436, L119
 Fiore, F., Massaro, E., Perola, G. C., & Piro, L. 1989, *ApJ*, 347, 171
 Greene, J., Bailyn, C. D., & Orosz, J. 2001, *ApJ*, 554, 1290
 Greiner, J., Cuby, J. G., & McCaughrean, M. J. 2001, *Nature*, 414, 522
 Hawley, J. F. 2000, *ApJ*, 528, 462
 Hawley, J. F., & Balbus, S. A. 1991, *ApJ*, 376, 223
 ———. 1992, *ApJ*, 400, 595
 Hawley, J. F., Gammie, C. F., & Balbus, S. A. 1995, *ApJ*, 440, 742
 Homan, J., Méndez, M., Wijnands, R., van der Klis, M., & van Paradijs, J. 1999, *ApJ*, 513, L119
 Homan, J., Wijnands, R., van der Klis, M., Belloni, T., van Paradijs, J., Klein-Wolt, M., Fender, R., & Méndez, M. 2001, *ApJS*, 132, 377
 Honma, F., Matsumoto, R., & Kato, S. 1992, *PASJ*, 44, 529
 Kalkofen, W., Rossi, P., Bodo, G., & Massaglia, S. 1994, *A&A*, 284, 976
 Kato, S. 1989, *PASJ*, 41, 745
 ———. 1990, *PASJ*, 42, 99
 ———. 2001, *PASJ*, 53, 1
 Kato, S., & Fukue, J. 1980, *PASJ*, 32, 377
 Kato, S., Fukue, J., & Mineshige, S. 1998, *Black-Hole Accretion Disks* (Kyoto: Kyoto Univ. Press)
 Koide, S. 2003, *Phys. Rev. D*, 67, 104010
 Koide, S., Kudoh, T., & Shibata, K. 1998, *ApJ*, 495, L63
 ———. 1999, *ApJ*, 522, 727
 Koide, S., Meier, D. L., Shibata, K., & Kudoh, T. 2000, *ApJ*, 536, 668
 Kuwabara, T., Shibata, K., Kudoh, T., & Matsumoto, R. 2000, *PASJ*, 52, 1109
 Lamb, F. K., Shibazaki, N., Alpar, A., & Shaham, J. 1985, *Nature*, 317, 681
 Lamb, H. 1932, *Hydrodynamics* (Cambridge: Cambridge Univ. Press)
 Lense, J., & Thirring, H. 1918, *Phys. Z.*, 19, 156
 Machida, M., Hayashi, M. R., & Matsumoto, R. 2000, *ApJ*, 532, L67
 Machida, M., & Matsumoto, R. 2003, *ApJ*, 585, 429
 Markwardt, C. B., Swank, J. H., & Taam, R. E. 1999, *ApJ*, 513, L37
 Matsumoto, R. 1999, in *Numerical Astrophysics*, ed. S. M. Miyama, K. Tomisaka, & T. Hanawa (Dordrecht: Kluwer), 195
 Matsumoto, R., Kato, S., & Honma, F. 1988, in *Physics of Neutron Stars and Black Holes*, ed. Y. Tanaka (Tokyo: Universal Academy Press), 155
 ———. 1989, in *Theory of Accretion Disks*, ed. F. Meyer, W. J. Duschl, J. Frank, & E. Meyer-Hofmeister (Dordrecht: Kluwer), 167
 Matsumoto, R., & Tajima, T. 1995, *ApJ*, 445, 767
 Matsumoto, R., Uchida, Y., Hirose, S., Shibata, K., Hayashi, M. R., Ferrari, A., Bodo, G., & Norman, C. 1996, *ApJ*, 461, 115
 Merloni, A., Vietri, M., Stella, L., & Bini, D. 1999, *MNRAS*, 304, 155
 Middleditch, J. 1982, *ApJ*, 257, L71
 Milsom, J. A., & Taam, R. E. 1997, *MNRAS*, 286, 358
 Mittaz, J. P. D., & Branduardi-Raymont, G. 1989, *MNRAS*, 238, 1029
 Morales-Rueda, L., Still, M. D., & Roche, P. 1999, *MNRAS*, 306, 753
 Morgan, E. H., Remillard, R. A., & Greiner, J. 1997, *ApJ*, 482, 993
 Nowak, M. A., & Lehr, D. E. 1998, in *Theory of Black Hole Accretion Disks*, ed. M. A. Abramowicz, G. Bjornsson, & J. E. Pringle (Cambridge: Cambridge Univ. Press), 148
 Nowak, M. A., & Wagoner, R. V. 1991, *ApJ*, 378, 656
 ———. 1992, *ApJ*, 393, 697
 Nowak, M. A., Wagoner, R. V., Begelman, M. C., & Lehr, D. E. 1997, *ApJ*, 477, L91
 Okazaki, A. T., Kato, S., & Fukue, J. 1987, *PASJ*, 39, 457
 Orosz, J. A., et al. 2002, *ApJ*, 568, 845
 Paczyński, B., & Wiita, P. J. 1980, *A&A*, 88, 23
 Patterson, J., Robinson, E. L., & Nather, R. E. 1977, *ApJ*, 214, 144
 Perez, C. A., Silbergleit, A. S., Wagoner, R. V., & Lehr, D. E. 1997, *ApJ*, 476, 589
 Remillard, R. A., McClintock, J. E., Sobczak, G. J., Bailyn, C. D., Orosz, J. A., Morgan, E. H., & Levine, A. M. 1999a, *ApJ*, 517, L127
 Remillard, R. A., Morgan, E. H., McClintock, J. E., Bailyn, C. D., & Orosz, J. A. 1999b, *ApJ*, 522, 397
 Rosen, S. R., Watson, T. K., Robinson, E. L., Prinja, R. K., Misselt, K., & Shafter, A. W. 1995, *A&A*, 300, 392
 Shahbaz, T., van der Hooft, F., Casares, J., Charles, P. A., & van Paradijs, J. 1999, *MNRAS*, 306, 89
 Shakura, N. I., & Sunyaev, R. 1973, *A&A*, 24, 337
 Sobczak, G. J., McClintock, J. E., Remillard, R. A., Bailyn, C. D., & Orosz, J. A. 1999, *ApJ*, 520, 776
 Sobczak, G. J., McClintock, J. E., Remillard, R. A., Cui, W., Levine, A. M., Morgan, E. H., Orosz, J. A., & Bailyn, C. D. 2000, *ApJ*, 531, 537
 Stella, L., & Vietri, M. 1998, *ApJ*, 492, L59
 Stella, L., Vietri, M., & Morsink, S. M. 1999, *ApJ*, 524, L63
 Stone, J. M., Hawley, J. F., Gammie, C. F., & Balbus, S. A. 1996, *ApJ*, 463, 656
 Stone, J. M., & Norman, M. L. 1994, *ApJ*, 433, 746
 Strohmayer, T. E. 2001a, *ApJ*, 552, L49
 ———. 2001b, *ApJ*, 554, L169
 Suematsu, Y., Shibata, K., Nishikawa, T., & Kitai, R. 1982, *Sol. Phys.*, 75, 99
 Tagger, M., Pellat, R., & Coroniti, F. V. 1992, *ApJ*, 393, 708
 Takeshima, T., Dotani, T., Mitsuda, K., & Nagase, F. 1994, *ApJ*, 436, 871
 Thorne, K. S., Price, R. H., & Macdonald, D. A. 1986, *Black Holes: The Membrane Paradigm* (New Haven: Yale Univ. Press)
 Tout, C. A., & Pringle, J. E. 1992, *MNRAS*, 259, 604
 van der Klis, M. 2000, *ARA&A*, 38, 717
 Vishniac, E. T., & Diamond, P. 1992, *ApJ*, 398, 561
 Wagoner, R. V. 1999, *Phys. Rep.*, 311, 259